Chapter 8
Characterization of Chemically Modified Gold/Silver Superatoms in the Gas Phase

Kiichirou Koyasu, Keisuke Hirata and Tatsuya Tsukuda

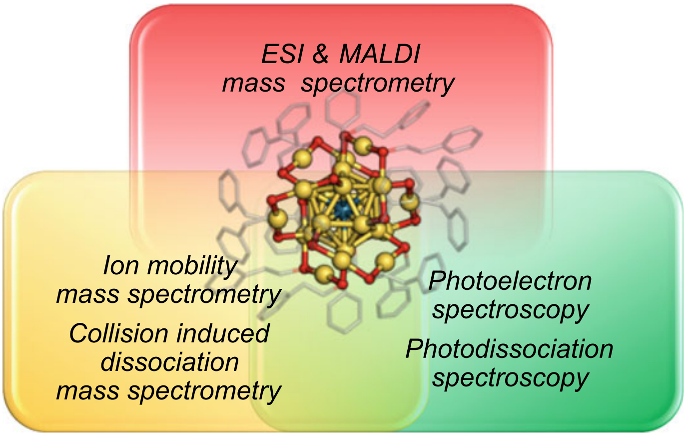

Characterization methods applied to ligand protected Au/Ag clusters in gas phase

© Springer Nature Singapore Pte Ltd. 2019
T. Ebata and M. Fujii (eds.), *Physical Chemistry of Cold Gas-Phase Functional Molecules and Clusters*,
https://doi.org/10.1007/978-981-13-9371-6_8

Abstract Atomically precise Au and Ag clusters protected by organic ligands can be viewed as chemically modified superatoms. These chemically modified Au/Ag superatoms have gained interests as promising building units of functional materials as well as ideal platforms to study the size-dependent evolution of structures and physicochemical properties. Mass spectrometry not only allows us to determine the chemical compositions of the synthesized superatoms but also gives us molecular-level insights into the mechanism of complex processes in solution. A variety of the gas-phase methods including ion-mobility–mass spectrometry, collision- or surface-induced dissociation mass spectrometry, photoelectron spectroscopy, and photodissociation mass spectrometry have been applied to the chemically modified Au/Ag superatom ions isolated in the gas phase. These studies have provided novel and complementary information on their intrinsic geometric and electronic structures that cannot be obtained by conventional characterization methods. This chapter surveys the recent progress in the gas-phase studies on chemically synthesized Au/Ag superatoms.

Keywords Ligand-protected gold/silver clusters · Superatoms · Mass spectrometry

8.1 Introduction

8.1.1 Metal Clusters as Novel Functional Units

Metal clusters composed of less than a few hundred atoms are located between the nanoparticles and atoms of the corresponding metal (Scheme 8.1) and have attracted the attention of scientists over the last four decades [1]. The central interest at the early stage of the research was observing the finite-size effects on the physical properties of metal clusters and understanding their origins from a microscopic viewpoint. To address these fundamental questions, versatile and efficient production methods for naked clusters (laser vaporization [2] and magnetron sputtering [3] methods) and ultrasensitive characterization methods coupled with mass spectrometry have been developed [4]. Experimental approaches for the study of size-specific properties of naked metal cluster ions are summarized in Fig. 8.1. Magic numbers were searched by mass spectrometry [4]. Electronic structures have been studied by photoelectron spectroscopy (PES) [5–10] and photodissociation spectroscopy (PDS) [11], whereas geometric structures (overall motif and atomic packing) have been studied by ion-mobility–mass spectrometry (IM MS) [12, 13], electron diffraction (ED) [14], and

---

K. Koyasu · K. Hirata · T. Tsukuda (✉)
Department of Chemistry, School of Science, The University of Tokyo, 7-3-1 Hongo, Bunkyo-Ku, Tokyo 113-0033, Japan
e-mail: tsukuda@chem.s.u-tokyo.ac.jp

K. Koyasu · T. Tsukuda
Elements Strategy Initiative for Catalysts and Batteries (ESICB), Kyoto University,
Katsura, Kyoto 615-8520, Japan

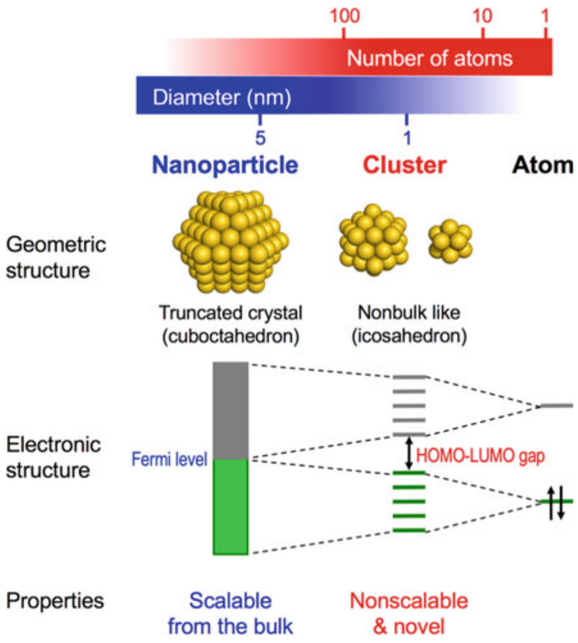

Scheme 8.1 Comparison between metal nanoparticles and metal clusters

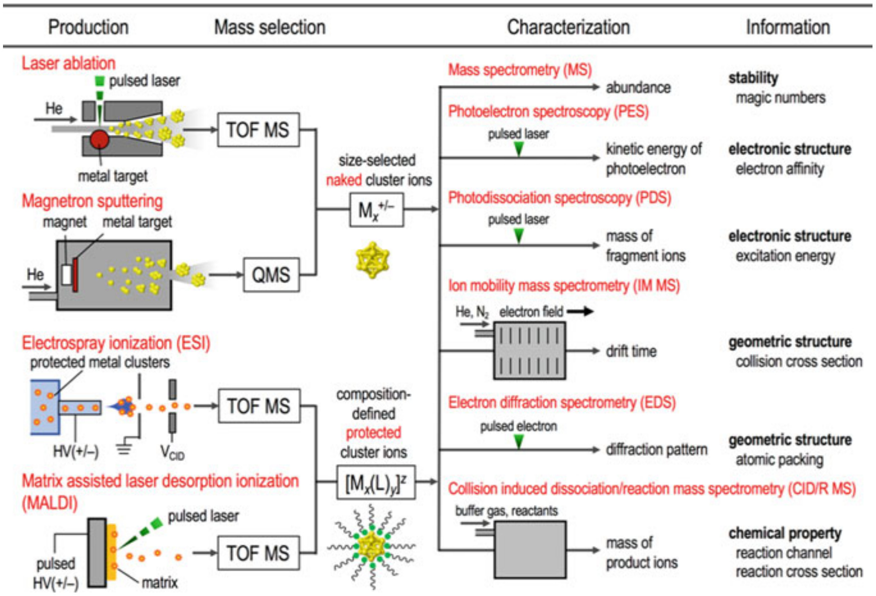

Fig. 8.1 Summary of experimental approaches for the investigation of size-selected naked metal cluster ions and composition-defined protected metal cluster ions

vibrational spectroscopy [15]. Chemical properties and binding strength were studied by collision-induced dissociation/reaction mass spectrometry (CID/CIR MS) [16, 17]. These experimental results with the help of theoretical calculations have led to discoveries of a variety of remarkable size-specific phenomena and physicochemical properties. For example, observations of magic numbers in the size distributions have led to the concept of electron shell closing based on the Jellium model [18] and superatoms [19]. It is widely recognized that various physicochemical properties of metal clusters deviate significantly from their bulk counterparts due to the unique geometric and electronic structures (Scheme 8.1) and evolve dramatically as a function of size, as exemplified by the metal–insulator transition [20]. Rapid progress in the research under the catchphrases, "small is different" [21, 22] and "every atom counts" [23, 24], has convinced the community that metal clusters are promising functional units of novel materials.

8.1.2 Naked Gold Clusters as Prototypical Superatoms

Since the discovery of oxidation catalysis of nanosized gold (Au) by Haruta [25], Au clusters have been the most extensively studied systems among the naked metal clusters [4–17]. Here, the knowledge on the structures and properties of Au clusters accumulated so far is summarized as a reference to that for chemically synthesized Au clusters. The stability of Au clusters is governed by the electronic structure: Au clusters gain a special stability when superatomic electronic shells (1S, 1P, 1D, 2S, 1F, 2P, 1G, 2D,...) are closed with valence electrons totaling 2, 8, 18, 20, 34, 40, 58, and so on [4, 26]. Neutral Au_n clusters with $n = 20, 34, 40, 58, \ldots$ correspond to magic clusters since each Au atom provides a single 6s electron as a valence electron. Electronic shell closure at these magic clusters manifests itself in the remarkably smaller electron affinity (EA) than those of the neighboring sizes (Fig. 8.2a) [4–6, 9, 26]. The size-dependent and size-specific chemical reactivity toward molecular oxygen [17], relevant to aerobic oxidation catalysis [27], is also correlated with the electronic structure (Fig. 8.2b): the molecular adsorption proceeds via electron transfer from Au_n^- into the adsorbed π^* of O_2. Small Au_n clusters exhibit diverse, non-FCC structures and unexpected evolution in geometric structures [26]. Figure 8.2c plots the collision cross section (CCSs) of Au_n^- as a function of size n. The decrease in the CCSs at $n = 13$ is explained in terms of the structural transition from planar to three-dimensional motifs [13, 28]. Au_{13} takes neither cuboctahedral nor icosahedral structures [7]. The magic Au_{20} has an FCC structure with a pyramidal motif [6], while Au_{34} and Au_{58} have $Au_4@Au_{30}$ [9, 26] and $Au_{10}@Au_{48}$ [29] core–shell structures, respectively (Fig. 8.2c). We can see that these magic Au clusters provide nearly spherical potential wells for the confinement of the valence electrons. Although the FCC structure appears at $n = 20$ after hollow cage structures in the size range of 16–18 [8], hollow structures appear again at $n = 21$ and 24 [14].

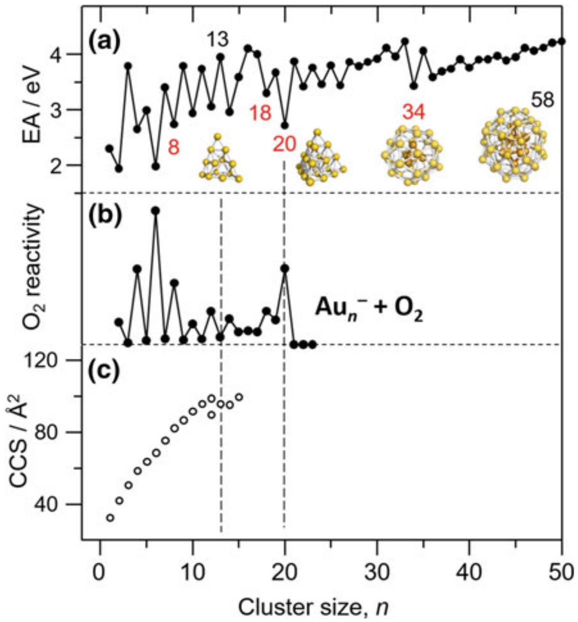

Fig. 8.2 Size dependence of **a** AEA of naked Au$_n$ and **b** reactivity and **c** CCS of naked Au$_n^-$ [5, 13, 17]. Inset shows theoretically predicted structures of Au$_{13}$, Au$_{20}$, Au$_{34}$, and Au$_{58}$

8.1.3 Ligand-Protected Gold Clusters as Chemically Modified Superatoms

Chemical synthesis has been a challenge for developing the materials science of metal clusters, as evidenced by the explosive growth in the materials science of nanocarbons after the large-scale production of C_{60} by Smalley and Krätschmer [30]. Au clusters have been studied most extensively as representative systems of the chemical synthesis because of their robustness against oxidation under ambient conditions. The first requirement for the chemical synthesis is to stabilize individual Au clusters against aggregation so that they can be treated as conventional chemical compounds. To this end, the surface of the Au cluster has been passivated by ligands L, such as thiolates (RS) [31], alkynes (RC≡C) [32], phosphines (R_3P) [33], carbenes [34], and halides to yield $[Au_xL_y]^z$. The second requirement is to define the chemical composition of $[Au_xL_y]^z$ with atomic and molecular precision. In recent decades, a large variety of $[Au_xL_y]^z$ with atomically defined sizes in the range of x < ~500 have been synthesized [35–38]. The nonbulk-like atomic packing of the Au cores has been elucidated by single-crystal X-ray diffraction (SCXRD) analysis and transmission electron microscopy [39]. The discrete nature of the electronic structures has been demonstrated by UV–Vis optical spectroscopy, photoluminescence, and voltammetry. Figure 8.3 lists single-crystal structures and the optical absorption spectra of representative small Au- or Ag-based clusters protected by ligands

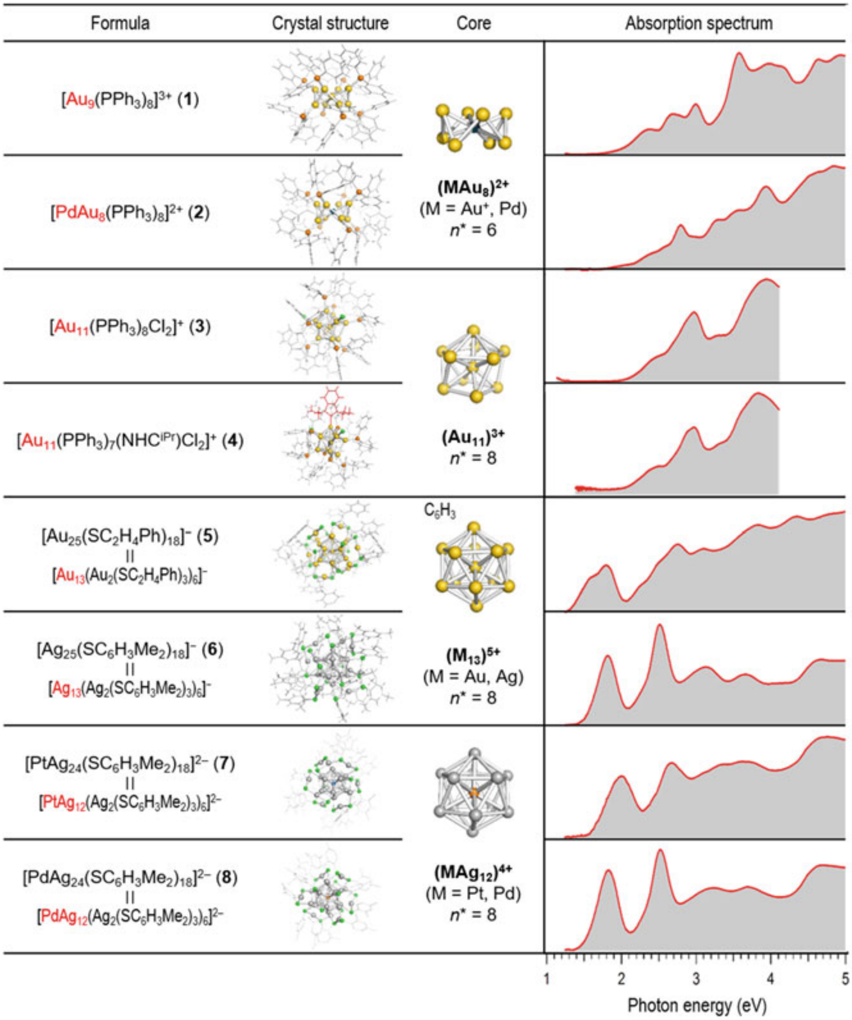

Fig. 8.3 Geometric structures determined by single-crystal X-ray diffraction, core structures, and optical spectra of $[Au_9(PPh_3)_8]^{3+}$ (**1**), $[PdAu_8(PPh_3)_8]^{2+}$ (**2**), $[Au_{11}(PPh_3)_8Cl_2]^{+}$ (**3**), $[Au_{11}(PPh_3)_7(NHC^{iPr})Cl_2]^{+}$ (**4**), $[Au_{25}(SC_2H_4Ph)_{18}]^{-}$ (**5**), $[Ag_{25}(SC_6H_3Me_2)_{18}]^{-}$ (**6**), $[PtAg_{24}(SC_6H_3Me_2)_{18}]^{2-}$ (**7**), and $[PdAg_{24}(SC_6H_3Me_2)_{18}]^{2-}$ (**8**). The red wireframe in **4** represents an N-heterocyclic carbene ligand

$[(\mathrm{Au/Ag})_x\mathrm{L}_y]^z$. The structures of the metallic cores are highlighted in the figure. $[\mathrm{Au_9(PPh_3)_8}]^{3+}$ (**1**) [40] and $[\mathrm{PdAu_8(PPh_3)_8}]^{2+}$ (**2**) [41] have a crown-shaped M@$\mathrm{Au_8}$ (M = Au, Pd) core with the unligated M atom at the center. $[\mathrm{Au_{11}(PPh_3)_8Cl_2}]^{+}$ (**3**) [42] has a quasi-icosahedral $\mathrm{Au_{11}}$ core protected by mixed ligands of Cl and $\mathrm{PPh_3}$, whereas one of the $\mathrm{PPh_3}$ ligands of **3** is replaced with N-heterocyclic carbene ($\mathrm{NHC^{iPr}}$) to form $[\mathrm{Au_{11}(PPh_3)_7(NHC^{iPr})Cl_2}]^{+}$ (**4**) [34]. $[\mathrm{Au_{25}(SC_2H_4Ph)_{18}}]^{-}$ (**5**) [43] and $[\mathrm{Ag_{25}(SC_6H_3Me_2)_{18}}]^{-}$ (**6**) [44] have icosahedral cores of $\mathrm{Au_{13}}$ and $\mathrm{Ag_{13}}$, respectively, protected by six $\mathrm{M_2(SR)_3}$ (M = Au, Ag) bidentate units with staple motifs. The central Ag atom of the $\mathrm{Ag_{13}}$ core of **6** is replaced with a Pt and Pd atom to form $[\mathrm{PtAg_{24}(SC_6H_3Me_2)_{18}}]^{2-}$ (**7**) and $[\mathrm{PdAg_{24}(SC_6H_3Me_2)_{18}}]^{2-}$ (**8**), respectively [45].

The ligands not only sterically protect the Au/Ag-based core from aggregation but also adjust the number of valence electrons in the Au/Ag cores and the atomic packing of the Au/Ag cores. A simple electron counting scheme has been proposed for $[\mathrm{Au}_x\mathrm{L}_y]^z$ [46]. The formal number of valence electrons (n*) in the Au core is calculated by the following equation:

$$n^* = x - y \times N - z \tag{8.1}$$

where x represents the total number of valence electrons supplied by Au constituent atoms and is equal to the number of the Au atoms in the cluster. The N value is the number of electrons taken from the Au core by a single ligand L, which is dependent on the nature of the Au–L interaction. A thiolate, alkynyl, or halogen ligand takes one electron ($N = 1$), whereas a phosphine or carbene ligand does not take any electrons ($N = 0$). The n^* values of $[\mathrm{Au}_x\mathrm{L}_y]^z$ adopt the values of 8, 18, 20, 34, 40, 58, and so on as long as the Au core can be viewed as a sphere. This simple counting scheme can be applied to bimetallic $[(\mathrm{Au/Ag})_x\mathrm{L}_y]^z$ clusters and the analogues doped with Pd or Pt [47, 48]: each Ag atom provides one valence electron, whereas Pd and Pt atoms do not. The n^* values thus calculated are 6 for **1** and **2** and 8 for **3**–**8** (Fig. 8.3). Thus, the crown-shaped $(\mathrm{M@Au_8})^{2+}$ (M = $\mathrm{Au^+}$, Pd) cores in **1** and **2** can be viewed as oblate-shaped superatoms, where three 1P superatomic orbitals are split into two subgroups. Two of the 1P superatomic orbitals ($\mathrm{1P_x}$, $\mathrm{1P_y}$) correspond to HOMO and the $\mathrm{1P_z}$ superatomic orbital to LUMO. In contrast, the quasi-icosahedral $(\mathrm{Au_{11}})^{3+}$ cores of **3** and **4**, icosahedral $(\mathrm{M_{13}})^{5+}$ cores of **5** (M = Au) and **6** (M = Ag), and $(\mathrm{M@Ag_{12}})^{4+}$ (M = Pt, Pd) cores of **7** and **8** can be viewed as nearly spherical superatoms. The 1P and 1D superatoms of **3**–**8** correspond to the HOMO and LUMO, respectively. Figure 8.3 also presents optical absorption spectra, showing clear absorption onsets and well-resolved structures due to the quantized electronic structures. The onsets for **3**–**8** are assigned to HOMO (1P)–LUMO (1D) transition, whereas those for **1** and **2** are not due to the HOMO ($\mathrm{1P_x}$, $\mathrm{1P_y}$)–LUMO ($\mathrm{1P_z}$) transitions because it is optically forbidden.

A variety of the gas-phase methods have been applied to the chemically modified Au/Ag superatoms including **1**–**8** by introducing them in the gas phase using electrospray ionization (ESI) or matrix-assisted laser desorption/ionization (MALDI) method (Fig. 8.1). These studies have provided novel and complementary information on their intrinsic geometric and electronic structures that cannot be obtained by conventional characterization methods. This chapter examines the recent progress in the gas-phase studies on chemically synthesized Au/Ag-based clusters $[(\mathrm{Au/Ag})_x\mathrm{L}_y]^z$.

8.2 Mass Spectrometry (MS)

Mass spectrometry plays several important roles in the gas-phase studies on $[(\mathrm{Au/Ag})_x\mathrm{L}_y]^z$: (1) determination of chemical compositions and net charge, which are the key descriptors of $[(\mathrm{Au/Ag})_x\mathrm{L}_y]^z$; (2) detection and identification of intermediate species formed in solution during the formation and reactions of the clusters; and (3) as an interface for the gas-phase measurements listed in Fig. 8.1. The key requirement is the ionization of the chemically synthesized clusters in the intact form. To this end, the conventional methods such as ESI [49] and MALDI [50] have been used. This section showcases typical examples of mass spectrometric characterization of the synthesized products and mass spectrometric detection of reaction intermediates.

8.2.1 Experimental Methods

Schematic setups for the ESI and MALDI mass spectrometry (ESI/MALDI MS) are shown in Fig. 8.1. $[(\mathrm{Au/Ag})_x\mathrm{L}_y]^z$ intrinsically charged ($z \neq 0$) in solution like **1**–**8** can be directly introduced into the mass spectrometer as a continuous (cw) beam by desolvation in the ESI source. The ESI method can be applied even to neutral clusters ($z = 0$) if they are charged either by the protonation or deprotonation of the ligands before ESI or attachment of cationic species such as Cs^+ during ESI. The ESI method also allows us to sample intermediate and transient species nascently formed in solution. In contrast, a pulsed beam of $[(\mathrm{Au/Ag})_x\mathrm{L}_y]^z$ can be generated by the MALDI method: solidified cluster samples with a matrix (most typically DCTB) are irradiated with a pulsed laser light. The MALDI method is also used to desorb Au clusters stabilized by polymer [51]. Portions of the cw ion beam from the ESI source or the pulsed ion beams from the MALDI source are injected into the TOF MS by applying a pulsed electric field.

8.2.2 Mass and Charge Determination of Synthesized Clusters

Determination of the chemical compositions and charge states of the isolated clusters is the primary purpose of mass spectrometry. Since the first successful application to a series of Au clusters protected by glutathione (GSH) [49], mass spectrometry has been widely and routinely used to check the purity of the synthesized cluster samples. Figure 8.4a, b shows the first successful applications: the ESI mass spectrum for $[Au_{25}(SG)_{18-x}(SG^{-})_{x}]^{-}$, where x represents the number of the deprotonated GS ligands (SG^{-}), and the MALDI mass spectrum for $[Au_{25}(SC_2H_4Ph)_{18}]^{-}$ (**5**), respectively [50]. In Fig. 8.4a, the $[Au_{25}(SG)_{18-x}(SG^{-})_{x}]^{-}$ clusters are multiply charged due to the multiple deprotonations of the SG ligands. Figure 8.4c shows the ESI and MALDI mass spectra of $Au_{940\pm20}(SC_2H_4Ph)_{160\pm4}$, which is among the largest clusters (core diameter of 2.9 nm) studied by mass spectrometry so far [52]. MALDI MS has also been successfully applied to characterization of the Au clusters stabilized by polyvinylpyrrolidone (PVP). Figure 8.4d demonstrates the formation of Au_{34} magic clusters and doping of a single Rh atom [53, 54].

8.2.3 Characterization of Transient Clusters in Solution

Another important application of MS is the detection of transient species produced in solution, which will provide fundamental information on the reaction mechanism at the molecular level [55–63]. During the formation of $[Au_{25}(SG)_{18}]^{-}$, 29 stable intermediate species were detected by retarding the reduction rate of Au(I) precursors using CO as the reducing agent [55]. All the intermediates featured even-numbered valence electrons and their sequential appearance indicated a 2 e^{-} reduction growth mechanism. In situ ESI MS has been applied to a variety of solution processes: the seed-mediated growth of $[Au_{25}(SR)_{18}]^{-}$ to $[Au_{44}(SR)_{26}]^{-}$ [56]; alloying process between $[Au_2(SR)_2Cl]^{-}$ complexes and $[Ag_{44}(SR)_{30}]^{4-}$ [57]; ligand-exchange-induced size transformation of $Au_{38}(SC_2H_4Ph)_{24}$ to $Au_{36}(SC_6H_4(t\text{-Bu}))_{24}$ [58]; intercluster reaction between $[Au_{25}(SC_2H_4Ph)_{18}]^{-}$ (**5**) and $[Ag_{44}(SC_6H_4F)_{30}]^{4-}$ [59]; and spontaneous alloying between $[Au_{25}(SC_2H_4Ph)_{18}]^{-}$ (**5**) and $[Ag_{25}(SC_6H_3Me_2)_{18}]^{-}$ (**6**) [60]. In the last reaction, the formation of dianionic species $[Ag_{25}Au_{25}(SC_6H_3Me_2)_{18}(SC_2H_4Ph)_{18}]^{2-}$ was elucidated at the initial stage (Fig. 8.5).

The formation of hydride (H^{-}) adduct $[HPdAu_8(PPh_3)_8]^{+}$ was observed in the ESI mass spectrum of the reaction mixture of $[PdAu_8(PPh_3)_8]^{2+}$ (**2**) with $NaBH_4$ (Fig. 8.6a) [61]:

$$\left[PdAu_8(PPh_3)_8\right]^{2+}(\mathbf{2}) + H^{-} \rightarrow \left[HPdAu_8(PPh_3)_8\right]^{+} \tag{8.2}$$

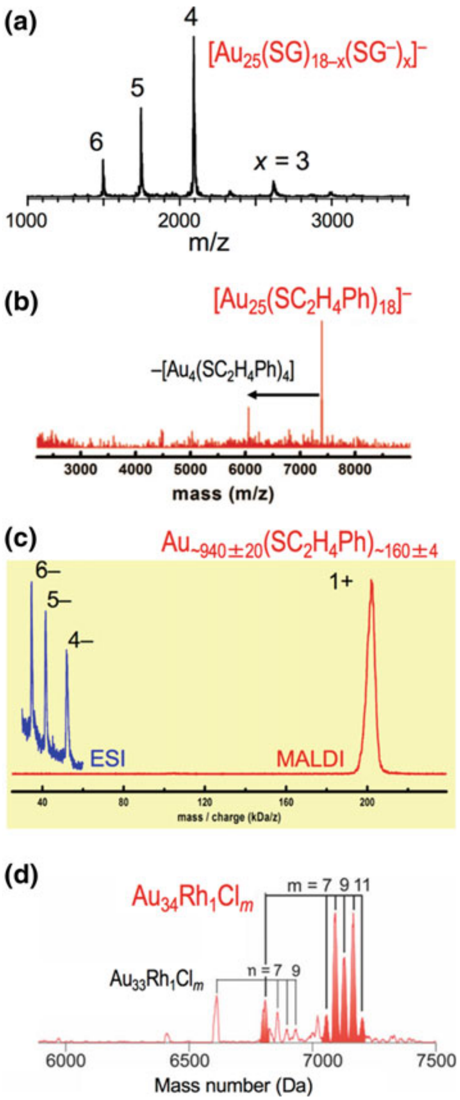

Fig. 8.4 Negative-mode **a** ESI mass spectrum of $[Au_{25}(SG)_{18-x}(SG^-)_x]^-$ (Adapted with permission from Ref. [49]. Copyright (2005) American Chemical Society.) and **b** MALDI mass spectrum of $[Au_{25}(SC_2H_4Ph)_{18}]^-$ (**5**). (Adapted with permission from Ref. [50]. Copyright (2008) American Chemical Society.) **c** Negative-mode ESI and positive-mode MALDI mass spectra of $Au_{940\pm 20}(SC_2H_4Ph)_{160\pm 4}$. (Adapted with permission from Ref. [52]. Copyright (2014) American Chemical Society.) **d** Negative-mode MALDI mass spectra of Rh-doped Au:PVP clusters (Ref. [54]—Reproduced by permission of The Royal Society of Chemistry)

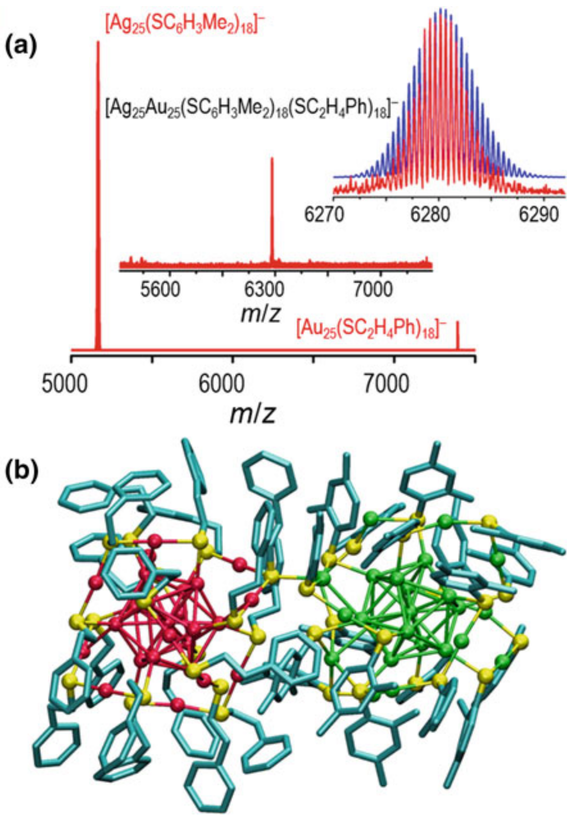

Fig. 8.5 a ESI mass spectrum of the mixture of $[Au_{25}(SC_2H_4Ph)_{18}]^-$ (**5**) and $[Ag_{25}(SC_6H_3Me_2)_{18}]^-$ (**6**) and **b** DFT-optimized structure of $[Ag_{25}Au_{25}(SC_6H_3Me_2)_{18}(SC_2H_4Ph)_{18}]^{2-}$ (Reprinted from Ref. [60] by The Author(s) licensed under CC BY 4.0)

Theoretical studies suggested that the hydride is adsorbed onto the unligated central Pd atom of $[PdAu_8(PPh_3)_8]^{2+}$ (**2**) (Fig. 8.3). Time-resolved ESI mass spectra during the reactions of $[HPdAu_8(PPh_3)_8]^+$ with Au(I)Cl(PPh_3) revealed the formation of $[HPdAu_{10}(PPh_3)_8Cl_2]^+$ via $[HPdAu_9(PPh_3)_8Cl]^+$ (Fig. 8.6b) while retaining the n^* value of eight:

$$\left[HPdAu_8(PPh_3)_8\right]^+ + AuCl \rightarrow \left[HPdAu_9(PPh_3)_8Cl\right]^+ \tag{8.3}$$

$$\left[HPdAu_9(PPh_3)_8Cl\right]^+ + AuCl \rightarrow \left[HPdAu_{10}(PPh_3)_8Cl_2\right]^+ \tag{8.4}$$

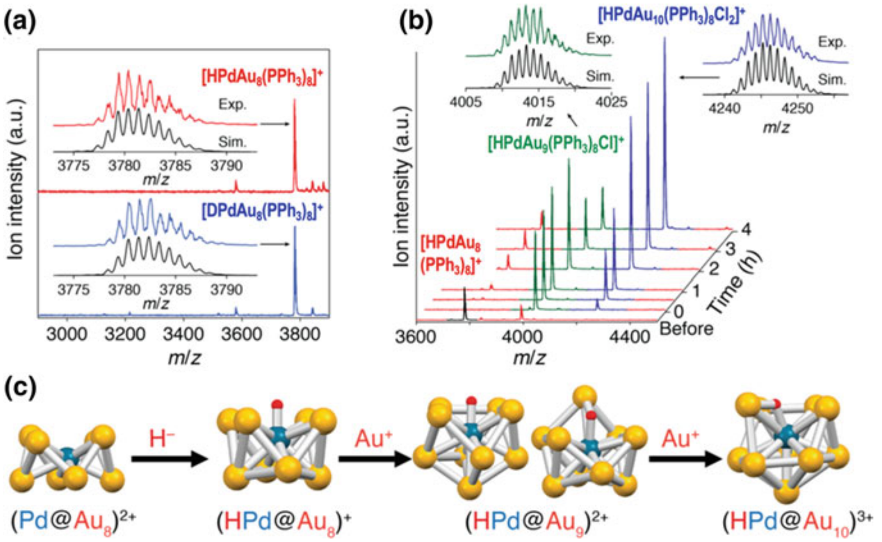

Fig. 8.6 **a** ESI mass spectra of the mixture of $[PdAu_8(PPh_3)_8]^{2+}$ (**2**) and $NaBH_4$ or $NaBD_4$. **b** Time-resolved ESI mass spectra recorded after mixing $[HPdAu_8(PPh_3)_8]^+$ and $AuClPPh_3$. **c** Core structures of the DFT-optimized structures of $[PdAu_8(PMe_3)_8]^{2+}$, $[HPdAu_8(PMe_3)_8]^+$, $[HPdAu_9(PMe_3)_8Cl]^+$, and $[HPdAu_{10}(PMe_3)_8Cl_2]^+$. The ligands are omitted for simplicity (Adapted with permission from Ref. [61]. Copyright 2018 American Chemical Society.)

The H atom remained bonded throughout the growth processes. The core structures during the hydride-mediated growth reactions (8.2)–(8.4) are summarized in Fig. 8.6c. This hydride-mediated growth process is different from that of $[Au_9(PPh_3)_8]^{3+}$ (**1**) to $[Au_{11}(PPh_3)_8Cl_2]^+$ (**3**), where the hydrogen is lost in the form of a proton at the first stage of the growth [62]:

$$\left[Au_9(PPh_3)_8\right]^{3+}(\mathbf{1}) + H^- \rightarrow \left[HAu_9(PPh_3)_8\right]^{2+} \tag{8.5}$$

$$\left[HAu_9(PPh_3)_8\right]^{2+} + AuCl \rightarrow \left[Au_{10}(PPh_3)_8Cl\right]^+ + H^+ \tag{8.6}$$

$$\left[Au_{10}(PPh_3)_8Cl\right]^+ + AuCl \rightarrow \left[Au_{11}(PPh_3)_8Cl_2\right]^+(\mathbf{3}) \tag{8.7}$$

These hydride-mediated growth processes represent a promising method of size-controlled synthesis based on the bottom-up approach [63].

8.3 Collision-Induced Dissociation Mass Spectrometry (CID MS)

In-source CID MS allows us to investigate the fragmentation patterns of $[(\mathrm{Au/Ag})_x\mathrm{L}_y]^z$ in the electronically ground state upon collisional activation with the atmospheric molecules. The fragmentation patterns provide information on the thermal stability of $[(\mathrm{Au/Ag})_x\mathrm{L}_y]^z$, the relative binding affinities of different ligands with respect to the clusters, and the effect of the ligand structure on their binding affinities.

8.3.1 Experimental Methods

A typical setup is schematically shown in Fig. 8.1. The cw beam of chemically purified $[(\mathrm{Au/Ag})_x\mathrm{L}_y]^z$ ions from the ESI source is introduced into a differentially pumped area in which the typical pressure is approximately several hundred Pa. Isolated ions $[(\mathrm{Au/Ag})_x\mathrm{L}_y]^z$ undergo dissociation upon collision with the buffer gas:

$$\left[(\mathrm{Au/Ag})_x\mathrm{L}_y\right]^z \to [(\mathrm{Au/Ag})_m\mathrm{L}_n]^z + \text{neutral fragments} \tag{8.8}$$

The voltage applied to the electrodes in the differentially pumped area (V_{CID} in Fig. 8.1) is adjusted to control the nominal collision energy of the $[(\mathrm{Au/Ag})_x\mathrm{L}_y]^z$ ions with the background gas: the collision energy increases with the $\mathrm{V}_{\mathrm{CID}}$.

8.3.2 Fragmentations from Synthesized Clusters

In the CID of the representative phosphine-protected Au cluster $[\mathrm{Au}_{11}(\mathrm{PPh}_3)_8\mathrm{Cl}_2]^+$ (**3**), the loss of the $\mathrm{AuCl(PPh_3)}$ units proceeded competitively with that of the $\mathrm{PPh_3}$ ligands (Fig. 8.7a, Eqs. 8.9 and 8.10) [64].

$$\left[\mathrm{Au}_{11}(\mathrm{PPh}_3)_8\mathrm{Cl}_2\right]^+(\mathbf{3}) \to \begin{cases} \left[\mathrm{Au}_{11}(\mathrm{PPh}_3)_{8-n}\mathrm{Cl}_2\right]^+ + n\,\mathrm{PPh}_3 & (8.9) \\ \left[\mathrm{Au}_{11-m}(\mathrm{PPh}_3)_{8-m}\mathrm{Cl}_{2-m}\right]^+ + m\,\mathrm{AuCl(PPh}_3) & (8.10) \end{cases}$$

The numbers of released $\mathrm{PPh_3}$ and $\mathrm{AuCl(PPh_3)}$ units increased with the increase in the collision energy (Fig. 8.7a). According to Eq. 8.1, the n^* values in the daughter ions formed in Eqs. 8.9 and 8.10 are calculated to be eight, which agrees with that predicted by the electronic shell model. The direct loss of anionic ligand Cl^- while

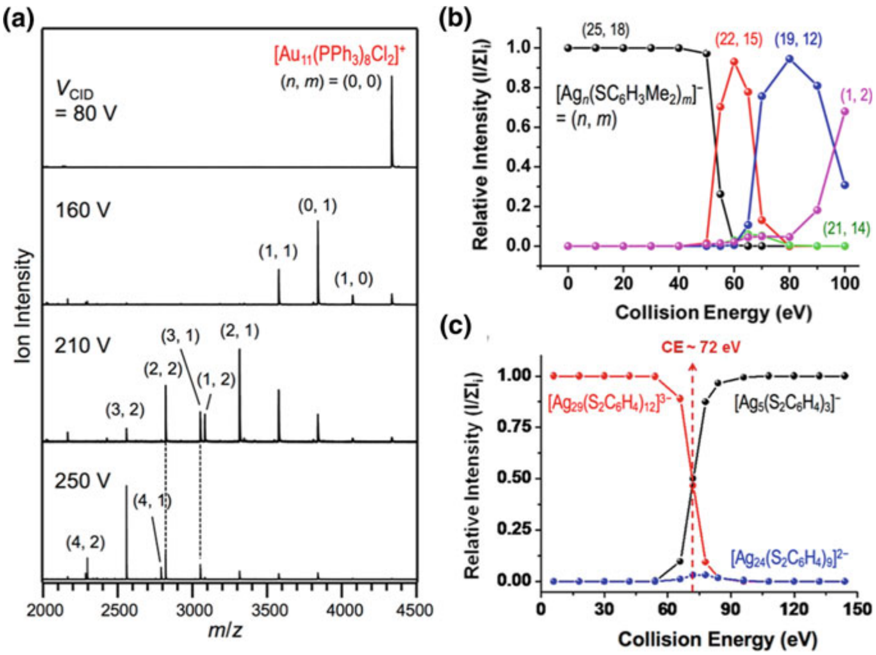

Fig. 8.7 **a** A typical CID mass spectrum of $[Au_{11}(PPh_3)_8Cl_2]^+$ (**3**) as a function of the CID voltage (V_{CID}) (Adapted with permission from Ref. [64]. Copyright 2018 American Chemical Society). The notation (n, m) represents the numbers of released PPh_3 and $AuCl(PPh_3)$ units. Collision energy-resolved fragmentation curves of **b** $[Ag_{25}(SC_6H_3Me_2)_{18}]^-$ (**6**) and **c** $[Ag_{29}(S_2C_6H_4)_{12}]^{3-}$ (Adapted with permission from Ref. [69]. Copyright 2017 American Chemical Society)

leaving the daughter ions with nine electrons did not proceed, indicating that the heterolytic dissociation of the Au–Cl bond is not energetically favored. These results revealed that the CID pathways are governed by the electronic stability of the daughter ions.

In the low-energy CID of the representative thiolate-protected Au cluster $[Au_{25}(SC_2H_4Ph)_{18}]^-$ (**5**), $[Au_{21}(SC_2H_4Ph)_{14}]^-$ was formed as a major daughter ion by losing an $Au_4(SC_2H_4Ph)_4$ unit (Eq. 8.11) [65, 66]. The loss of an $Au_4(SR)_4$ unit is commonly observed not only in the CID of other $[Au_x(SR)_y]^{+/-}$ clusters [67] but also in the MALDI of $[Au_x(SR)_y]$ recorded under high laser fluence [50]. Theoretical calculations predicted that the dissociation of $[Au_{25}(SMe)_{18}]^-$ into $[Au_{21}(SMe)_{14}]^-$ and $Au_4(SMe)_4$ is exothermic only by 0.82 eV and proceeds via complex rearrangement of the intracluster chemical bonds [68]. The preferential loss of $Au_4(SC_2H_4Ph)_4$ was ascribed to the electronic stability of the daughter anion $[Au_{21}(SC_2H_4Ph)_{14}]^-$ ($n^* = 8$) and the high stability of neutral fragment $Au_4(SC_2H_4Ph)_4$ with a cyclic structure. When the collision energy was further increased, loss of the second $Au_4(SC_2H_4Ph)_4$ as well as a $(C_2H_4Ph)_2$ unit was observed (Eqs. 8.12 and 8.13):

$$\left[\mathrm{Au_{25}(SC_2H_4Ph)_{18}}\right]^{-}(\mathbf{5}) \rightarrow \left[\mathrm{Au_{21}(SC_2H_4Ph)_{14}}\right]^{-} + \mathrm{Au_4(SC_2H_4Ph)_4} \tag{8.11}$$

$$\left[\mathrm{Au_{21}(SC_2H_4Ph)_{14}}\right]^{-} \rightarrow \begin{cases} \left[\mathrm{Au_{21}(SC_2H_4Ph)_{12}S_2}\right]^{-} + \mathrm{(C_2H_4Ph)_2} & (8.12) \\ \left[\mathrm{Au_{17}(SC_2H_4Ph)_{10}}\right]^{-} + \mathrm{Au_4(SC_2H_4Ph)_4} & (8.13) \end{cases}$$

The n^* values in the daughter ions in Eqs. 8.12 and 8.13 are eight if we consider that two electrons are removed by an S_2 unit. This estimation supports the conclusion that the CID channels are governed by the electronic stability of the daughter ions.

Thiolate-protected Ag clusters such as $[\mathrm{Ag_{25}(SC_6H_3Me_2)_{18}}]^-$ (**6**), $[\mathrm{Ag_{29}(S_2C_6H_4)_{12}}]^{3-}$, and $[\mathrm{Ag_{44}(SC_6H_4F)_{30}}]^{4-}$ exhibit different CID patterns from the Au analogues. $[\mathrm{Ag_{25}(SC_6H_3Me_2)_{18}}]^-$ (**6**) undergoes sequential loss of an $\mathrm{Ag_3(SR)_3}$ unit (Fig. 8.7b, Eqs. 8.14 and 8.15) [69]:

$$\left[\mathrm{Ag_{25}(SC_6H_3Me_2)_{18}}\right]^{-}(\mathbf{6}) \rightarrow \left[\mathrm{Ag_{22}(SC_6H_3Me_2)_{15}}\right]^{-} + \mathrm{Ag_3(SC_6H_3Me_2)_3} \tag{8.14}$$

$$\left[\mathrm{Ag_{22}(SC_6H_3Me_2)_{15}}\right]^{-} \rightarrow \left[\mathrm{Ag_{19}(SC_6H_3Me_2)_{12}}\right]^{-} + \mathrm{Ag_3(SC_6H_3Me_2)_3} \tag{8.15}$$

The above fragmentation pathways are determined by the electronic stability of the daughter ions ($n^* = 8$) and the geometric stability of $\mathrm{Ag_3(SC_6H_3Me_2)_3}$ units. $[\mathrm{Ag_{29}(S_2C_6H_4)_{12}}]^{3-}$ dissociates into two anionic fragments (Fig. 8.7c, Eqs. 8.16 and 8.17):

$$\left[\mathrm{Ag_{29}(S_2C_6H_4)_{12}}\right]^{3-} \rightarrow \left[\mathrm{Ag_{24}(S_2C_6H_4)_9}\right]^{2-} + \left[\mathrm{Ag_5(S_2C_6H_4)_3}\right]^{-} \tag{8.16}$$

$$\left[\mathrm{Ag_{24}(S_2C_6H_4)_9}\right]^{2-} \rightarrow \left[\mathrm{Ag_{19}(S_2C_6H_4)_4}\right]^{-} + \left[\mathrm{Ag_5(S_2C_6H_4)_3}\right]^{-} \tag{8.17}$$

Both of the fragments $[\mathrm{Ag_{24}(S_2C_6H_4)_9}]^{2-}$ and $[\mathrm{Ag_{19}(S_2C_6H_4)_4}]^-$ of Eqs. 8.16 and 8.17 are eight electron systems. $[\mathrm{Ag_{44}(SC_6H_4F)_{30}}]^{4-}$ ($n^* = 18$) dissociates into $[\mathrm{Ag_{43}(SC_6H_4F)_{28}}]^{3-}$ ($n^* = 18$) and $[\mathrm{Ag_1(SC_6H_4F)_2}]^-$:

$$\left[\mathrm{Ag_{44}(SC_6H_4F)_{30}}\right]^{4-} \rightarrow \begin{cases} \left[\mathrm{Ag_{43}(SC_6H_4F)_{28}}\right]^{3-} + \left[\mathrm{Ag_1(SC_6H_4F)_2}\right]^{-} & (8.18) \\ \left[\mathrm{Ag_{42}(SC_6H_4F)_{27}}\right]^{3-} + \left[\mathrm{Ag_2(SC_6H_4F)_3}\right]^{-} & (8.19) \end{cases}$$

The CID pattern also provides the information on the relative binding affinity of the different ligands [71]. In the low-energy CID of $[\mathrm{Au_{11}(PPh_3)_7(NHC^{iPr})Cl_2}]^+$ (**4**), synthesized by replacing one of the $\mathrm{PPh_3}$ ligands of $[\mathrm{Au_{11}(PPh_3)_8Cl_2}]^+$ (**3**) with an N-heterocyclic carbene ($\mathrm{NHC^{iPr}}$), the loss of $\mathrm{NHC^{iPr}}$ was suppressed and that of $\mathrm{AuCl(NHC^{iPr})}$ or $\mathrm{AuCl(PPh_3)}$ was dominant (Eqs. 8.20 and 8.21) [34]:

$$\left[\mathrm{Au}_{11}(\mathrm{PPh}_3)_7\left(\mathrm{NHC}^{\mathrm{iPr}}\right)\mathrm{Cl}_2\right]^+(\mathbf{4}) \rightarrow \begin{cases} \left[\mathrm{Au}_{10}(\mathrm{PPh}_3)_7\mathrm{Cl}\right]^+ + \mathrm{AuCl}\left(\mathrm{NHC}^{\mathrm{iPr}}\right) & (8.20) \\ \left[\mathrm{Au}_{10}(\mathrm{PPh}_3)_6\left(\mathrm{NHC}^{\mathrm{iPr}}\right)\mathrm{Cl}\right]^+ + \mathrm{AuCl}(\mathrm{PPh}_3) & \end{cases} \tag{8.21}$$

This result demonstrates that NHC^{iPr} has significantly higher binding affinity to Au than PPh_3 through the strong Au–C bond [71].

The CID MS illustrates how the structures of the ligands affect by the interaction with the Au clusters. For example, the stability against CID processes was dependent on the position of carboxyl group on mercaptobenzoic acid used as protecting ligands of the Au_{25} clusters: the stability decreased in the order of $[Au_{25}(p\text{-}SC_6H_4CO_2H)_{18}]^-$ > $[Au_{25}(m\text{-}SC_6H_4CO_2H)_{18}]^-$ > $[Au_{25}(o\text{-}SC_6H_4CO_2H)_{18}]^-$ [72]. This trend was explained in terms of weakening of the Au–S bonds by the steric effect of the carboxyl group at the ortho position.

8.3.3 *Fragmentations from Transient Clusters in Solution*

In-source CID coupled with the ESI source also allows us to monitor the fragmentation pathways of the metal clusters produced in situ in solution. For example, all phosphine-protected Au clusters such as $[Au_{20}(PPh_3)_8]^{2+}$ [70] and $[Au_{11}(dppp)_5]^{3+}$ (dppp = 1,3-bis(diphenylphosphino)propane) [73] underwent dissociation of phosphine ligands (Eq. 8.22), indicating that the Au–P bonds are weakest within the systems (Fig. 8.8a, b):

$$\left[\mathrm{Au}_{20}(\mathrm{PPh}_3)_8\right]^{2+} \rightarrow \left[\mathrm{Au}_{20}(\mathrm{PPh}_3)_{8-n}\right]^{2+} + n\,\mathrm{PPh}_3 \tag{8.22}$$

The n^* values of the fragments are 18, illustrating the importance of electronic stability of the fragments. The PPh_3 ligands were sequentially lost up to $n = 4$ according to Eq. 8.22, but the loss of the fifth PPh_3 was significantly retarded. This suggests that eight PPh_3 ligands are divided into two groups in terms of the binding affinity to the Au_{20} core. This inference is consistent with the theoretical prediction that four PPh_3 ligands are weakly adsorbed on four (111) facets of the pyramidal Au_{20} core, while the remaining four PPh_3 ligands are more strongly coordinated to the apex sites of the Au_{20} core (Fig. 8.8c, d).

8.4 Ion-Mobility–Mass Spectrometry (IM MS)

IM MS determines the collision cross section (CCS) of $[(Au/Ag)_xL_y]^z$, which directly reflects the geometrical motif including the ligand layer (Fig. 8.1). Thus, IM MS also allows us to identify structural isomers if present and to monitor an isomerization process induced by collisional excitation.

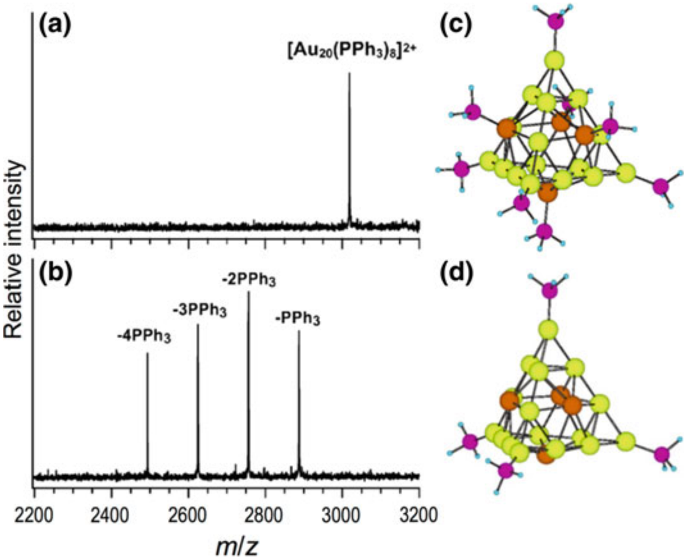

Fig. 8.8 **a** Mass spectrum and **b** CID mass spectrum of $[Au_{20}(PPh_3)_8]^{2+}$. The collision gas was benzene and the average collision energy was ~0.64 eV. DFT-optimized structures of **c** $[Au_{20}(PH_3)_8]^{2+}$ and **d** $[Au_{20}(PH_3)_4]^{2+}$ (Adapted with permission from Ref. [70]. Copyright 2004 American Chemical Society.)

8.4.1 Experimental Methods

In a commercially available apparatus (Synapt HDMS, Waters UK Ltd.), the mass-selected beam of $[(Au/Ag)_xL_y]^z$ prepared using the ESI source and a quadrupole mass filter is injected into the traveling wave ion mobility (TWIM) cell [74] by applying a pulsed voltage to a gate electrode. The $[(Au/Ag)_xL_y]^z$ ions in the TWIM cell are propelled by the continuous sequence of traveling waves with a triangular shape, but are unable to keep up with the wavefront in the presence of the buffer gas: larger ions spend longer drift time in the cell (T_{cell}). The experimental CCS Ω_{exp} is estimated by the following equation:

$$T_{\text{cell}} = \frac{\sqrt{\mu}}{z} A\Omega_{\text{exp}}^{B} \tag{8.23}$$

where the terms z and μ are the charge and the reduced mass of the clusters and the buffer gas, respectively. A and B are constants determined by calibration.

8.4.2 Morphology

The arrival time distribution (ATD) exhibited single peaks for $[Au_{25}(SC_2H_4Ph)_{18}]^-$ (**5**) [65] and binary clusters $[X@Ag_{14}(C\equiv CBu)_{12}]^+$ and $[X@Ag_8Cu_6(C\equiv CBu)_{12}]^+$ (X = Cl, Br), showing the absence of distinct isomers (Fig. 8.9a) [75]. Their experimental CCS values were, qualitatively, reproduced by those calculated based on their single-crystal structures. The agreement suggests that the clusters retain their geometrical motifs in the gas phase [65, 75]. The presence of two isomers in $[Au_8(PPh_3)_x(PPh_2Me)_{7-x}]^{2+}$ was identified from the doublet ATD profiles [76]. IM MS revealed the formation of the dimer of $[Au_{25}(SC_2H_4Ph)_{18}]^-$ (**5**) in solution, which cannot be identified by mass spectrometry based on the mass-to-charge ratio [77]. The following dimerization of $[Ag_{29}(S_2C_6H_4)_{12}]^{3-}$ mediated by alkali metal cations was observed by IM MS measurement (Fig. 8.9b) [78]:

$$2\left[Ag_{29}(S_2C_6H_4)_{12}\right]^{3-} + 2Na^+ \rightarrow \left[Ag_{29}(S_2C_6H_4)_{12}Na\right]_2^{4-} \tag{8.24}$$

8.4.3 Collision-Induced Isomerization

The CCSs of $[Au_9(PPh_3)_8]^{3+}$ (**1**) and $[PdAu_8(PPh_3)_8]^{2+}$ (**2**) having a crown motif (Fig. 8.10) in methanol electrosprayed into the gas phase were determined to be 442 and 422 Å^2, respectively [79]. The CCS values calculated for their single-crystal structures using the exact hard-sphere scattering method [80] were 413 and 420 Å^2, respectively. In contrast, those calculated using the projection approximation [81] and diffuse-hard-sphere scattering methods [82] deviate significantly from the experimental values, suggesting that it is not trivial to predict the packing structures of the clusters from the CCS values alone. The arrival time distributions of $[Au_9(PPh_3)_8]^{3+}$ (**1**) and $[PdAu_8(PPh_3)_8]^{2+}$ (**2**) were monitored by increasing the collision energy by reducing the He pressure in the cell to test the possibility of detecting structural isomers of $[Au_9(PPh_3)_8]^{3+}$ having the Au_9 cores with a butterfly motif [83]. $[Au_9(PPh_3)_8]^{3+}$ (**1**) and $[PdAu_8(PPh_3)_8]^{2+}$ (**2**) underwent isomerization to smaller species with the CCS values of 404 and 402 Å^2, respectively (Fig. 8.10). We interpret the results in terms of the collision-induced transformation of the ligand layer structures from the disordered phase into the densely packed phase due to CH–π and π–π interactions found in the single crystal. This observation suggests that the ESI allows the isolation of the clusters while retaining the structures including the ligand layers in dispersing media, which are determined by the subtle balance between ligand–solvent and ligand–ligand interactions.

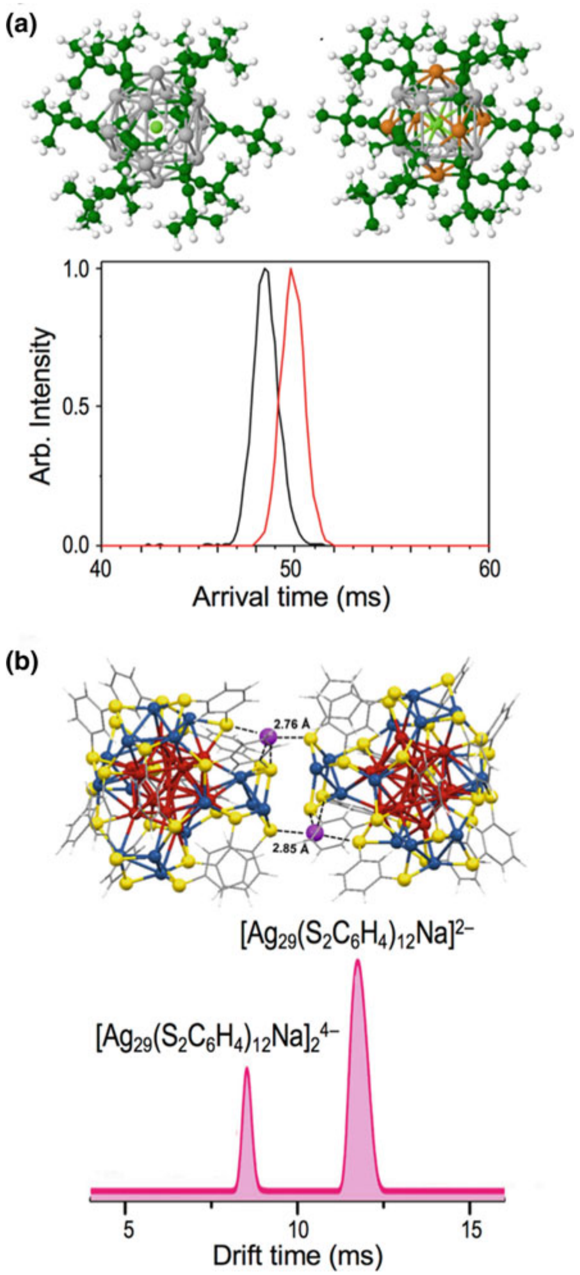

Fig. 8.9 **a** Arrival time distribution and DFT-optimized structures of $[Cl@Ag_{14}(C\equiv CBu)_{12}]^+$ and $[Cl@Ag_8Cu_6(C\equiv CBu)_{12}]^+$ (Reprinted with permission from Ref. [75]. Copyright 2017 American Chemical Society). **b** Arrival time distribution of $[Ag_{29}(S_2C_6H_4)_{12}Na]^{2-}$ and its dimer $[Ag_{29}(S_2C_6H_4)_{12}Na]_2^{4-}$. Inset shows the DFT-optimized structure of $[Ag_{29}(S_2C_6H_4)_{12}Na]_2^{4-}$ (Reproduced with permission of RSC Pub in the format Book via Copyright Clearance Center. From Ref. [78])

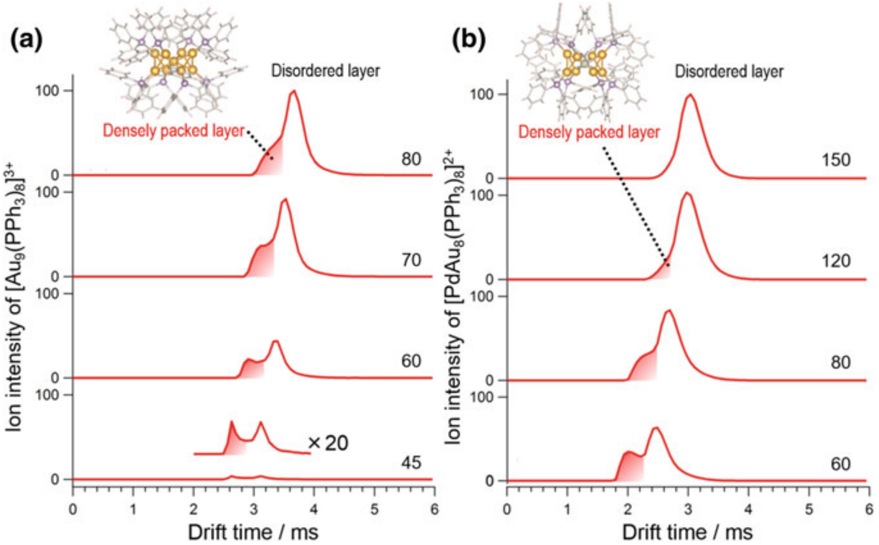

Fig. 8.10 Arrival time distributions of **a** $[Au_9(PPh_3)_8]^{3+}$ (**1**) and **b** $[PdAu_8(PPh_3)_8]^{2+}$ (**2**). The numbers indicate the He flow rates supplied to the cell in mL min^{-1} (Adapted with permission from Ref. [79]. Copyright 2018 American Chemical Society)

8.5 Photoelectron Spectroscopy (PES)

Photoelectron spectroscopy (PES) on negatively charged $[(Au/Ag)_xL_y]^z$ ($z < 0$) allows us to directly probe the electronic structures of occupied states: energy levels with respect to the vacuum level and density of states.

8.5.1 *Experimental Methods*

The negatively charged $[(Au/Ag)_xL_y]^z$ ($z < 0$) clusters from the ESI source are irradiated by pulsed laser light, after the mass selection (Fig. 8.1):

$$\left[(\mathrm{Au/Ag})_x\mathrm{L}_y\right]^z + h\,\nu \rightarrow \left[(\mathrm{Au/Ag})_x\mathrm{L}_y\right]^{z+1} + e^- \tag{8.25}$$

The kinetic energy of the photoelectron (E_{kin}) is determined by measuring the TOF of the electrons using a magnetic-bottle-type photoelectron spectrometer (MB PES), by which the photoelectrons detached toward all the solid angles are collected by an inhomogeneous magnetic field. The electron binding energy (E_{B}) is obtained by the energy conservation law expressed as

$$E_{\mathrm{B}} = E_{h[\nu]} - E_{\mathrm{kin}} \tag{8.26}$$

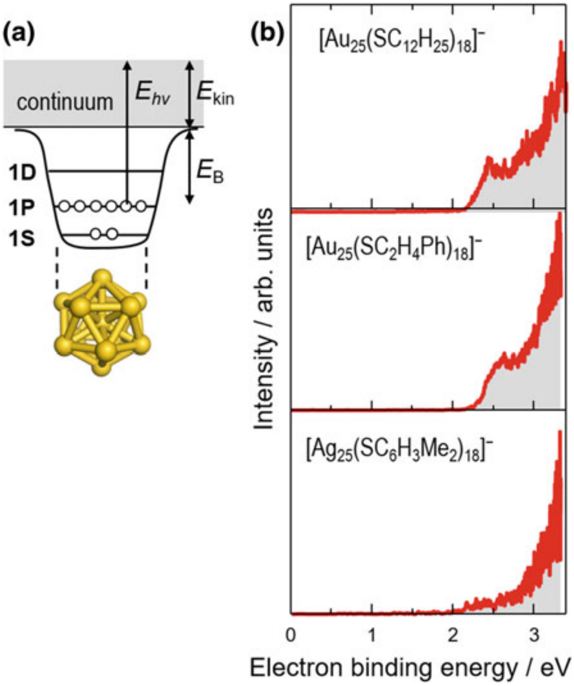

Fig. 8.11 **a** Schematic presentation of electronic structures of $(M_{13})^{5+}$ superatoms (M = Au, Ag). (Ref. [84, 85]—Reproduced by permission of The Royal Society of Chemistry). **b** PE spectra of $[Au_{25}(SC_{12}H_{25})_{18}]^-$ (Ref. [84]), $[Au_{25}(SC_2H_4Ph)_{18}]^-$ (**5**) (Ref. [85]), and $[Ag_{25}(SC_6H_3Me_2)_{18}]^-$ (**6**) (Ref. [85]) recorded at 355 nm

where $E_{h[\nu]}$ represents the photon energy (Fig. 8.11a).

8.5.2 Electron Affinities of $(M_{13})^{5+}$ (M = Au, Ag) Superatoms

Figure 8.11b shows the PE spectra of $[Au_{25}(SC_{12}H_{25})_{18}]^-$ [84], $[Au_{25}(SC_2H_4Ph)_{18}]^-$ (**5**) [85], and $[Ag_{25}(SC_6H_3Me_2)_{18}]^-$ (**6**) [85] recorded at 355 nm. The spectra of $[Au_{25}(SC_{12}H_{25})_{18}]^-$ and $[Au_{25}(SC_2H_4Ph)_{18}]^-$ (**5**) exhibit small humps and intense bands at the similar energies which are assigned to the photodetachment from the 1P superatomic orbital and Au 5*d* bands, respectively. Since SCXRD results showed that the structural difference between $[Au_{25}(SC_2H_4Ph)_{18}]^-$ and $[Au_{25}(SC_2H_4Ph)_{18}]^0$ is small [86], the spectral onset corresponds to the adiabatic electron affinity (AEA) of $[Au_{25}(SC_2H_4Ph)_{18}]^0$. The AEA values of $[Au_{25}(SC_{12}H_{25})_{18}]^0$ and $[Au_{25}(SC_2H_4Ph)_{18}]^0$ thus determined were 2.2 and 2.36 ± 0.01 eV, suggesting that the electronic structure of the superatomic $(Au_{13})^{5+}$ core is not affected seriously by the structures of the thiolates. These experimental AEA values are significantly smaller than those of a model system $[Au_{25}(SCH_3)_{18}]^0$ predicted theoretically (3.0 eV

[87] and 3.17 eV [88]). The PE spectrum of Ag analogues $[Ag_{25}(SC_6H_3Me_2)_{18}]^-$ (**6**) also exhibits two bands [85], which were assigned to the photodetachment from superatomic 1P orbitals and 4d orbitals localized on the Ag atoms, respectively. The AEA of $[Ag_{25}(SC_6H_3Me_2)_{18}]^0$ was determined to be 2.02 ± 0.01 eV, which is comparable to that of $[Au_{25}(SR)_{18}]^0$.

Doping of heteroatom(s) is a promising approach to enhancing the stability and further improving the properties of $[(Au/Ag)_xL_y]^z$. State-of-the-art synthesis based on coreduction and galvanic replacement allowed us to precisely define the number, element, and location of heteroatom(s) introduced into $[(Au/Ag)_xL_y]^z$ [89, 90]. For examples, $[Ag_{25}(SC_6H_3Me_2)_{18}]^-$ (**6**), $[PtAg_{24}(SC_6H_3Me_2)_{18}]^{2-}$ (**7**), and $[PdAg_{24}(SC_6H_3Me_2)_{18}]^{2-}$ (**8**) in Fig. 8.1 have $M@(Ag^+)_{12}$ ($M = Ag^+$, Pd, Pt) superatomic cores and provide an ideal platform to study the effect of single-atom doping on the electronic structures. PES measurements revealed that the binding energies of valence electrons in $M@(Ag^+)_{12}$ (M = Pd, Pt) were smaller than that in $(Ag^+)_{13}$ due to the reduction in formal charge of the core potential [91].

8.5.3 *Thermionic Emission from $(M_{13})^{5+}$ Superatoms*

The PE spectra of $[Au_{25}(SC_2H_4Ph)_{18}]^-$ (**5**) and $[Ag_{25}(SC_6H_3Me_2)_{18}]^-$ (**6**) recorded at 266 nm (Fig. 8.12a) exhibit completely different profiles from those at 355 nm (Fig. 8.11b). The PE spectra at 266 nm do not show the band structures observed at 355 nm (Fig. 8.11b) but are dominated by new bands at $E_B > 4.0$ eV. These findings indicate that slow electron emission dominates over direct photodetachment upon photoirradiation of $[Au_{25}(SC_2H_4Ph)_{18}]^-$ (**5**) and $[Ag_{25}(SC_6H_3Me_2)_{18}]^-$ (**6**) at 266 nm [85].

The emission of slow photoelectrons from the naked cluster anions of W, Nb, and Pt [92] has been observed and ascribed to thermionic emission (TE) from vibrationally excited anionic states. The absence of photoinduced TE from the naked cluster anions of Au and Ag was ascribed to their large VDEs and small vaporization energies in the corresponding bulk metal [92]. If the photon energy adsorbed (4.66 eV) is equally distributed to the vibrational degrees of freedom of the Au_{13} and Ag_{13} cores, the temperature of the core reaches 1.6×10^3 K. Kinetic energy distributions simulated at 1.6×10^3 K (black dotted lines in Fig. 8.12a) reproduce the experimentally observed profiles. This agreement supports the assignment to TE from the Au_{13} and Ag_{13} cores of $[Au_{25}(SC_2H_4Ph)_{18}]^-$ (**5**) and $[Ag_{25}(SC_6H_3Me_2)_{18}]^-$ (**6**), respectively. The above discussion suggests that the key to TE is the suppression of fragmentation of cluster anions electronically excited above the electron detachment threshold. The PD MS of $[Au_{25}(SC_2H_4Ph)_{18}]^-$ (**5**) and $[Ag_{25}(SC_6H_3Me_2)_{18}]^-$ (**6**) recorded at 266 nm were dominated by the depletion of parent ions: no photofragment ions from $[Au_{25}(SC_2H_4Ph)_{18}]^-$ (**5**) were observed, whereas $[Ag_{22}(SC_6H_3Me_2)_{15}]^-$ was observed as a minor fragment from $[Ag_{25}(SC_6H_3Me_2)_{18}]^-$ (**6**). These results indicate that the TE is a major decay pathway of $[M_{25}(SR)_{18}]^-$ (M = Au, Ag) photoexcited at 266 nm.

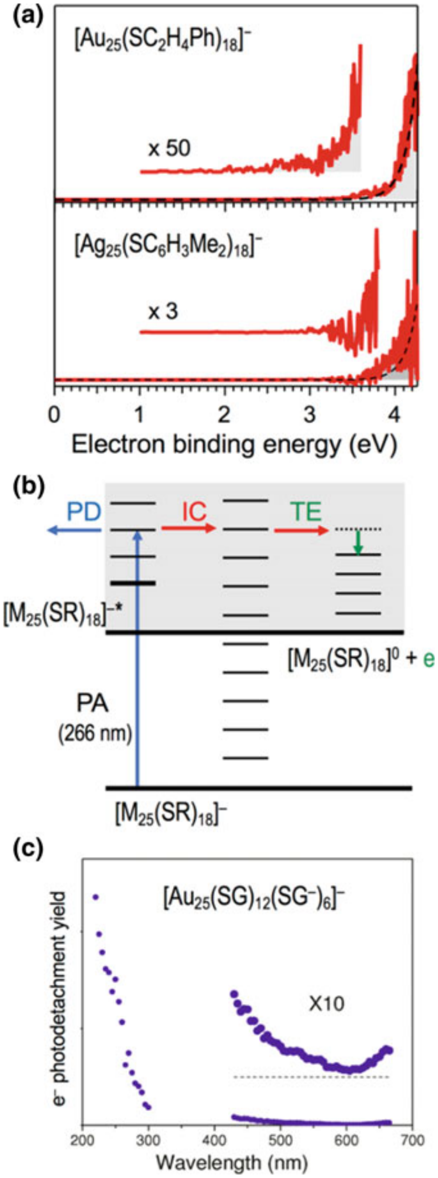

Fig. 8.12 **a** PE spectra of $[Au_{25}(SC_2H_4Ph)_{18}]^-$ (**5**) and $[Ag_{25}(SC_6H_3Me_2)_{18}]^-$ (**6**) recorded at 266 nm. Red solid and black dotted lines correspond to experimental data and simulated curves for thermionic emission of the M_{13} core, respectively [85]. **b** Jablonski diagram illustrating the TE pathway of $[M_{25}(SR)_{18}]^-$ following the photoexcitation at 266 nm. Horizontal lines are vibrational levels. Gray area indicates the electron detachment continuum. PA = photoabsorption; PD = photodissociation; IC = internal conversion; TE = thermionic emission [85]. (c) Electron photodetachment yield measured as a function of the laser wavelength for $[Au_{25}(SG)_{12}(SG^-)_6]^-$ (Adapted with permission from Ref. [85, 95]. Copyright 2010 American Chemical Society.)

The relaxation pathways of $[M_{25}(SR)_{18}]^-$ upon photoexcitation at 266 nm are explained by a Jablonski diagram (Fig. 8.12b). The initial step is selective excitation of $[M_{25}(SR)_{18}]^-$ into $[M_{25}(SR)_{18}]^{-*}$, which is embedded in the photodetachment continuum (shaded area in Fig. 8.12b). Electronic transitions within the M_{13} core as well as metal-to-ligand transitions [93] would be involved in the electronic transitions at 266 nm. Electronically excited $[M_{25}(SR)_{18}]^{-*}$ quickly undergoes internal conversion (IC) to form vibrationally excited $[M_{25}(SR)_{18}]^-$ followed by TE leaving internal energy in the remaining neutral $[M_{25}(SR)_{18}]^0$. Photodissociation, a competing process of IC, is almost completely suppressed even though the photon energy exceeds the energy required for dissociation into $[M_{21}(SR)_{14}]^-$ and $M_4(SR)_4$ (2.9 eV for M = Au) [68]. Protection of the M_{13} core by stiff $M_2(SR)_3$ units [94] may contribute to the promotion of the IC process of $[M_{25}(SR)_{18}]^{-*}$ by retarding the nuclear motion toward the dissociation. TE is also involved in the much more efficient photoelectron detachment from $[Au_{25}(SG)_{12}(SG^-)_6]^-$ at 200–300 nm than at 430–670 nm (Fig. 8.12c) [95].

8.6 Other Methods

This section briefly touches on other methods used for the characterization of $[(Au/Ag)_xL_y]^z$: photodissociation mass spectrometry (PD MS) and surface-induced dissociation mass spectrometry (SID MS).

8.6.1 Photodissociation Mass Spectrometry (PD MS)

Isolated ions $[(Au/Ag)_xL_y]^z$ undergo dissociation upon photoexcitation when the energy of absorbed laser light exceeds that required for dissociation:

$$\begin{aligned}\left[(\mathrm{Au/Ag})_x\mathrm{L}_y\right]^z + h\nu &\rightarrow \left[(\mathrm{Au/Ag})_x L_y\right]^{z\dagger}\\ &\rightarrow [(\mathrm{Au/Ag})_m\mathrm{L}_n]^z + \text{neutral fragments}\end{aligned} \tag{8.27}$$

Clusters in an electronically excited state $[(Au/Ag)_xL_y]^{z\dagger}$ may dissociate directly or undergo IC (Fig. 8.12b) followed by intracluster energy redistribution. Instead of detecting the depletion of the incident light as in the case of conventional spectroscopy in solution, the depletion of parent ions or the yield of daughter ions is monitored by mass spectrometry. The action spectra recorded as a function of the laser wavelength in principle correspond to the optical absorption spectra of $[(Au/Ag)_xL_y]^z$ isolated in gas phase. PD mass spectra can be measured by irradiating the chemically purified $[(Au/Ag)_xL_y]^z$ just before introduction into the mass spectrometer (Fig. 8.1) [85]. A unique feature of PD MS is that the energy deposited to the clusters is more precise and can be larger than that by CID. As a result, the PD at ultraviolet (UV) light results in richer fragmentation patterns compared to those by the CID method (Sect. 9.3).

Novel dissociation processes were found in the PD of $[\mathrm{Au_{25}(SC_6H_4CO_2H)_{18}}]^-(\mathrm{NH_4}^+)_3$ at 193 nm [96]. The initial stage of the PD was the sequential loss of ammonium salts leading to $[\mathrm{Au_{25}(SC_6H_4CO_2H)_{15}}]^{2+}$:

$$\begin{aligned}&\left[\mathrm{Au_{25}(SC_6H_4CO_2H)_{18}}\right]^-\left(\mathrm{NH_4^+}\right)_3 + h\nu(193\,\mathrm{nm})\\ &\rightarrow \left[\mathrm{Au_{25}(SC_6H_4CO_2H)_{18-x}}\right]^{-1+x}\left(\mathrm{NH_4^+}\right)_{3-x} + x(\mathrm{SC_6H_4CO_2H^-})\left(\mathrm{NH_4^+}\right), x = 1\text{–}3\end{aligned} \tag{8.28}$$

This step is followed by two competing fragmentation pathways:

$$\begin{aligned}&\left[\mathrm{Au_{25}(SC_6H_4CO_2H)_{15}}\right]^{2+} + h\nu(193\,\mathrm{nm})\\ &\rightarrow \begin{cases}\left[\mathrm{Au_{25}S_y(SC_6H_4CO_2H)_{15-2y}}\right]^{2+} + y\,\mathrm{S(C_6H_4CO_2H)_2}, & y = 1\text{–}7 \quad (8.29)\\ \left[\mathrm{Au_{25}S_{2y}(SC_6H_4CO_2H)_{15-2y}}\right]^{2+} + y\,\mathrm{(C_6H_4CO_2H)_2}, & y = 1\text{–}7 \quad (8.30)\end{cases}\end{aligned}$$

These PD processes (8.28)–(8.30) lead to nearly complete removal of the thiolates while retaining the total number of Au atoms. This phenomenon is similar to the observation of $[\mathrm{Au_{25}S_{\sim12}}]^-$ in the laser desorption process of $[\mathrm{Au_{25}(SC_2H_4Ph)_{18}}]^-$ (**5**) [97]. Also observed in the PD MS was $[\mathrm{Au_4(SC_6H_4CO_2H)_4} + \mathrm{Na}]^+$, which may be produced via vibrationally excited states in the electronically ground state as in the case of the CID processes.

8.6.2 Surface-Induced Dissociation (SID)

Surface-induced dissociation (SID) is another method used to study the dissociation processes of $[(\mathrm{Au/Ag})_x\mathrm{L}_y]^z$. It has been demonstrated that ~10% of the collisional energy can be deposited into a projectile by collision with a solid surface on a timescale of femtoseconds [98]. Since the collision energy of the ionic species can be easily tuned over a wide range, collision with the surface can impart much larger energy than that by PD and CID. Efficient and ultrafast energy conversion may promote further fragmentation of $[(\mathrm{Au/Ag})_N(\mathrm{L})_M]^Z$. It is reported that multiply charged phosphine-protected Au clusters, such as $[\mathrm{Au_7(PPh_3)_6}]^{2+}$, $[\mathrm{Au_8(PPh_3)_6}]^{2+}$, $[\mathrm{Au_8(PPh_3)_7}]^{2+}$, and $[\mathrm{Au_9(PPh_3)_7}]^{2+}$, underwent fissions into ionic fragments in addition to loss of a neutral $\mathrm{PPh_3}$ [99]:

$$\left[\mathrm{Au_7(PPh_3)_6}\right]^{2+} \rightarrow \left[\mathrm{Au_6(PPh_3)_4}\right]^+ + \left[\mathrm{Au_1(PPh_3)_2}\right]^+ \tag{8.31}$$

The results showed strong contrast to the results of CID measurement on the similar system, in which the loss of a neutral $\mathrm{PPh_3}$ was mainly observed [99]. However, the interpretation of the SID mass spectra is not straightforward due to the concurrent charge transfer processes between the projectiles and surfaces. For example, charge stripping from $[Ag_{11}(SG)_7]^{3-}$ was observed upon the collision with a self-assembled monolayer of a fluorocarbon on the gold surface [100]. It was proposed that this charge stripping is associated with the release of anionic fragments, such as $Ag(SG)^-$ and $Ag_4(SG)_3^-$.

8.7 Summary

This chapter summarizes the recent progress in the gas-phase studies on ligand-protected Au/Ag clusters $[(Au/Ag)_xL_y]^z$ synthesized in solution with atomic precision.

Mass spectrometry (MS) coupled with soft ionization such as electrospray ionization (ESI) and matrix-assisted laser desorption/ionization (MALDI) methods has been routinely used to determine the chemical compositions of $[(Au/Ag)_xL_y]^z$. Another important application of MS is the in situ detection of transient species produced in solution, which will help the molecular-level understanding of the mechanism of complex processes in solutions: seed- or hydride-mediated growth processes, alloying processes, ligand exchange reactions, ligand-exchange-induced size transformation, and metal exchange reactions between the clusters. Novel intermediates such as hydride-doped clusters and dimers of the clusters were observed.

Collision-induced dissociation (CID) MS allows us to investigate the fragmentation patterns of $[(Au/Ag)_xL_y]^z$ upon collisional activation with the gaseous molecules. The fragmentation patterns provide information on the thermal stability of $[(Au/Ag)_xL_y]^z$, the relative binding affinities of different ligands with respect to the clusters, and the effect of the ligand structure on their binding affinities.

Ion-mobility (IM) MS determines the collision cross section (CCS) of $[(Au/Ag)_xL_y]^z$, which directly reflects the geometrical motif including the ligand layer. IM MS also allows us to identify structural isomers if present and to monitor an isomerization process induced by collisional excitation.

Photoelectron spectrometry (PES) on negatively charged $[(Au/Ag)_xL_y]^z$ ($z < 0$) allows us to directly probe the electronic structures of occupied states: energy levels with respect to the vacuum level and density of states. Thiolate-protected Au/Ag clusters exhibit thermionic emission upon UV laser irradiation, whereas naked Au/Ag clusters do not.

The characterization of $[(Au/Ag)_xL_y]^z$ in the gas phase will elucidate their intrinsic geometric and electronic structures in the absence of the perturbation from the environments. Future studies with a combination with the gas-phase methods and the conventional methods such as single-crystal X-ray crystallography and X-ray absorption spectroscopy [101] will deepen our understanding on the structures–properties correlations of $[(Au/Ag)_xL_y]^z$ and contribute to the development of the materials science of chemically modified superatoms.

References

1. Haberland, H. (ed.): Clusters of Atoms and Molecules. Springer, Berlin (1994)
2. Dietz, T.G., Duncan, M.A., Powers, D.E., Smalley, R.E.: Laser production of supersonic metal cluster beams. J. Chem. Phys. **74**, 6511 (1981); Bondybey, V.E., English, J.H.: Laser induced fluorescence of metal clusters produced by laser vaporization: gas phase spectrum of Pb_2. J. Chem. Phys. **74**, 6978 (1982)
3. Haberland, H., Karrais, M., Mall, M.: A new type of cluster and cluster ion source. Z. Phys. D **20**, 413 (1991)
4. de Heer, W.A.: The physics of simple metal clusters: experimental aspects and simple models. Rev. Mod. Phys. **65**, 611 (1993)
5. Taylor, K.J., Pettiette-Hall, C.L., Cheshnovsky, O., Smalley, R.E.: Ultraviolet photoelectron spectra of coinage metal clusters. J. Chem. Phys. **96**, 3319 (1992)
6. Li, J., Li, X., Zhai, H.-J., Wang, L.-S.: Au_{20}: a tetrahedral cluster. Science **299**, 864 (2003)
7. Häkkinen, H., Yoon, B., Landman, U., Li, X., Zhai, H.-J., Wang, L.-S.: On the electronic and atomic structures of small Au_n^- (N = 4–14) clusters: a photoelectron spectroscopy and density-functional study. J. Phys. Chem. A **107**, 6168 (2003)
8. Bulusu, S., Li, X., Wang, L.-S., Zeng, X.C.: Evidence of hollow golden cages. Proc. Natl. Acad. Sci. **103**, 8326 (2006)
9. Lechtken, A., Schooss, D., Stairs, J.R., Blom, M.N., Furche, F., Morgner, N., Kostko, O., von Issendorff, B., Kappes, M.M.: $Au_{34}{}^-$: a chiral gold cluster? Angew. Chem., Int. Ed. **46**, 2944 (2007)
10. Huang, W., Ji, M., Dong, C.-D., Gu, X., Wang, L.-M., Gong, X.G., Wang, L.-S.: Relativistic effects and the unique low-symmetry structures of gold nanoclusters. ACS Nano **2**, 897 (2008)
11. Gilb, S., Jacobsen, K., Schooss, D., Furche, F., Ahrichs, R., Kappes, M.M.: Electronic photodissociation spectroscopy of $Au_n^-\cdot Xe$ ($n = 7$–11) versus time-dependent density functional theory prediction. J. Chem. Phys. **121**, 4619 (2004)
12. Glib, S., Weis, P., Furche, F., Ahlrichs, R., Kappes, M.M.: Structures of small gold cluster cations (Au_n^+, $n < 14$): ion mobility measurements versus density functional calculations. J. Chem. Phys. **116**, 4094 (2002)
13. Furche, F., Ahlrichs, R., Weis, P., Jacob, C., Gilb, S., Bierweiler, T., Kappes, M.M.: The structures of small gold cluster anions as determined by a combination of ion mobility measurements and density functional calculations. J. Chem. Phys. **117**, 6982 (2002)
14. Xing, X., Yoon, B., Landman, U., Parks, J.H.: Structural evolution of Au nanoclusters: from planar to cage to tubular motifs. Phys. Rev. B **74**, 165423 (2006)
15. Gruene, P., Rayner, D.M., Redlich, B., van der Meer, A.F.G., Lyon, J.T., Meijer, G., Fielicke, A.: Structures of neutral Au_7, Au_{19}, and Au_{20} clusters in the gas phase. Science **321**, 674 (2008)
16. St. Becker, Dietrich, G., Hase, H.-U., Kluge, H.-J., Kreisle, D., St. Krücheberg, Lindinger, M., Lützenkirchen, K., Weidele, H., Ziegler, J.: Collision induced dissociation of stored gold cluster ions. Z. Phys. D **30**, 341 (1994)
17. Wallace, W.T., Whetten, R.L.: Coadsorption of CO and O_2 on selected gold clusters: evidence for efficient room-temperature CO_2 generation. J. Am. Chem. Soc. **124**, 7499 (2002)
18. Cohen, M.L., Chou, M.Y., Knight, W.D., de Heer, W.A.: Physics of metal clusters. J. Phys. Chem. **91**, 3141 (1987)
19. Castleman, A.W., Khanna, S.N.: Clusters, superatoms, and building blocks of new materials. J. Phys. Chem. C **113**, 2664 (2009)
20. Issendorff, B., Cheshnovsky, O.: Metal to insulator transitions in clusters. Annu. Rev. Phys. Chem. **56**, 549 (2005)
21. El-Sayed, M.A.: Small is different: shape-, size-, and composition-dependent properties of some colloidal semiconductor nanocrystals. Acc. Chem. Res. **37**, 326 (2004)
22. Landman, U., Luedtke, W.D.: Small is different: energetic, structural, thermal, and mechanical properties of passivated nanocluster assemblies. Faraday Discuss. **125**, 1 (2004)

23. Heiz, U., Sanchez, A., Abbet, S., Schneider, W.D.: Catalytic oxidation of carbon monoxide on monodispersed platinum clusters: each atom counts. J. Am. Chem. Soc. **121**, 3214 (1999)
24. Landman, U.: Materials by numbers: computations as tools of discovery. Proc. Natl. Acad. Sci. **102**, 6671 (2005)
25. Haruta, M., Kobayashi, T., Sano, H., Yamada, N.: Novel gold catalysts for the oxidation of carbon monoxide at a temperature far below 0 °C. Chem. Lett. **16**, 405 (1987)
26. Wang, L.-M., Wang, L.-S.: Probing the electronic properties and structural evolution of anionic gold clusters in the gas phase. Nanoscale **4**, 4038 (2012)
27. Yamazoe, S., Koyasu, K., Tsukuda, T.: Nonscalable oxidation catalysis of gold clusters. Acc. Chem. Res. **47**, 816 (2014)
28. Weis, P.: Structure determination of gaseous metal and semi-metal cluster ions by ion mobility spectrometry. Int. J. Mass Spectrom. **245**, 1 (2005)
29. Ouyang, R., Xie, Y., Jiang, D.-E.: Global minimization of gold clusters by combining neural network potentials and the basin-hopping method. Nanoscale **7**, 14817 (2015)
30. Parker, D.H., Wurz, P., Chatterjee, K., Lykke, K.R., Hunt, J.E., Pellin, M.J., Hemminger, J.C., Gruen, D.M., Stock, L.M.: High-yield synthesis, separation, and mass-spectrometric characterization of fullerenes C_{60} to C_{266}. J. Am. Chem. Soc. **113**, 7499 (1991)
31. Whetten, R.L., Khoury, J.T., Alvarez, M.M., Murthy, S., Vezmar, I., Wang, Z.L., Stephens, P.W., Cleveland, C.L., Luedtke, W.D., Landman, U.: Nanocrystal gold molecules. Adv. Mater. **8**, 428 (1996)
32. Maity, P., Tsunoyama, H., Yamauchi, M., Xie, S., Tsukuda, T.: Organogold clusters protected by phenylacetylene. J. Am. Chem. Soc. **133**, 20123 (2011)
33. Schmid, G. (ed.), Nanoparticles: From Theory to Application, 2nd, Completely Revised and Updated Ed. (Wiley, New Jersey, 2010)
34. Narouz, M.R., Osten, K.M., Unsworth, P.J., Man, R.W.Y., Salorinne, K., Takano, S., Tomihara, R., Kaappa, S., Malola, S., Dinh, C.-T., Padmos, J.D., Ayoo, K., Garrett, P.J., Nambo, M., Horton, J.H., Sargent, E.H., Häkkinen, H., Tsukuda, T., Crudden, C.M.: ***N***-Heterocyclic carbene-functionalized magic number gold nanoclusters. Nature Chem. **11**, 419 (2019)
35. Tsukuda, T.: Toward an atomic-level understanding of size-specific properties of protected and stabilized gold clusters. Bull. Chem. Soc. Jpn. **85**, 151 (2012)
36. Tsukuda, T., Häkkinen, H. (eds.): Protected metal clusters: from fundamentals to applications. Elsevier, Amsterdam (2015)
37. Jin, R., Zeng, C., Zhou, M., Chen, Y.: Atomically precise colloidal metal nanoclusters and nanoparticles: fundamentals and opportunities. Chem. Rev. **116**, 10346 (2016)
38. Chakraborty, I., Pradeep, T.: Atomically precise clusters of noble metals: emerging link between atoms and nanoparticles. Chem. Rev. **117**, 8208 (2017)
39. Azubel, M., Koivisto, J., Malola, S., Bushnell, D., Hura, G.L., Koh, A.L., Tsunoyama, H., Tsukuda, T., Pettersson, M., Häkkinen, H., Kornberg, R.D.: Electron microscopy of gold nanoparticles at atomic resolution. Science **345**, 909 (2014)
40. Bellon, P.L., Cariati, F., Manassero, M., Naldini, L., Sansoni, M.: Novel gold clusters. Preparation, properties, and x-ray structure determination of salts of octakis(triarylphosphine)enneagold, $[Au_9L_8]X_3$. J. Chem. Soc. D 1423 (1971)
41. Matsuo, S., Takano, S., Yamazoe, S., Koyasu, K., Tsukuda, T.: Selective and high-yield synthesis of oblate superatom $[PdAu_8(PPh_3)_8]^{2+}$. ChemElectroChem **3**, 1206 (2016)
42. McKenzie, L.C., Zaikova, T.O., Hutchison, J.E.: Structurally similar triphenylphosphine-stabilized undecagolds, $Au_{11}(PPh_3)_7Cl_3$ and $[Au_{11}(PPh_3)_8Cl_2]Cl$, exhibit distinct ligand exchange pathways with glutathione. J. Am. Chem. Soc. **136**, 13426 (2014)
43. Heaven, M.W., Dass, A., White, P.S., Holt, K.M., Murray, R.M.: Crystal structure of the gold nanoparticle $[N(C_8H_{17})_4][Au_{25}(SCH_2CH_2Ph)_{18}]$. J. Am. Chem. Soc. **130**, 3754 (2008)
44. Joshi, C.P., Bootharaju, M.S., Alhilaly, M.J., Bakr, O.M.: $[Ag_{25}(SR)_{18}]^-$: the "golden" silver nanoparticle. J. Am. Chem. Soc. **137**, 11578 (2015)
45. Yan, J., Su, H., Yang, H., Malola, S., Lin, S., Häkkinen, H., Zheng, N.: Total structure and electronic structure analysis of doped thiolated silver $[MAg_{24}(SR)_{18}]^{2-}$ (M = Pd, Pt) clusters. J. Am. Chem. Soc. **137**, 11880 (2015)

46. Walter, M., Akola, J., Lopez-Acevedo, O., Jadzinsky, P.D., Calero, G., Ackerson, C.J., Whetten, R.L., Grönbeck, H., Häkkinen, H.: A unified view of ligand-protected gold clusters as superatom complexes. Proc. Natl. Acad. Sci. **105**, 9157 (2008)
47. Kwak, K., Tang, Q., Kim, M., Jiang, D.-E., Lee, D.: Interconversion between superatomic 6-electron and 8-electron configurations of $M@Au_{24}(SR)_{18}$ clusters (M = Pd, Pt). J. Am. Chem. Soc. **137**, 10833 (2015)
48. Liu, Y., Chai, X., Cai, X., Chen, M., Jin, R., Ding, W., Zhu, Y.: Central doping of a foreign atom into the silver cluster for catalytic conversion of CO_2 toward C–C bond formation. Angew. Chem., Int. Ed. **57**, 9775 (2018)
49. Negishi, Y., Nobusada, K., Tsukuda, T.: Glutathione-protected gold clusters revisited: bridging the gap between Gold(I)−Thiolate complexes and Thiolate-protected gold nanocrystals. J. Am. Chem. Soc. **127**, 5261 (2005)
50. Dass, A., Stevenson, A., Dubay, G.R., Tracy, J.B., Murray, R.W.: Nanoparticle MALDI-TOF mass spectrometry without fragmentation: $Au_{25}(SCH_2CH_2Ph)_{18}$ and mixed monolayer $Au_{25}(SCH_2CH_2Ph)_{18-x}(L)_x$. J. Am. Chem. Soc. **130**, 5940 (2008)
51. Tsunoyama, H., Tsukuda, T.: Magic numbers of gold clusters stabilized by PVP. J. Am. Chem. Soc. **131**, 18216 (2009)
52. Kumara, C., Zuo, X., Cullen, D.A., Dass, A.: Faradaurate-940: synthesis, mass spectrometry, electron microscopy, high-energy x-ray diffraction, and x-ray scattering study of $Au_{\sim 940\pm 20}(SR)_{\sim 160\pm 4}$ nanocrystals. ACS Nano **8**, 6431 (2014)
53. Hayashi, S., Ishida, R., Hasegawa, S., Yamazoe, S., Tsukuda, T.: Doping a single palladium atom into gold superatoms stabilized by PVP: emergence of hydrogenation catalysis. Top. Catal. **61**, 136 (2018)
54. Hasegawa, S., Takano, S., Yamazoe, S., Tsukuda, T.: Prominent hydrogenation catalysis of a PVP-stabilized Au_{34} superatom provided by doping a single Rh atom. Chem. Commun. **54**, 5915 (2018)
55. Luo, Z.T., Nachammai, V., Zhang, B., Yan, N., Leong, D.T., Jiang, D.E., Xie, J.P.: Toward understanding the growth mechanism: tracing all stable intermediate species from reduction of Au(I)–Thiolate complexes to evolution of Au_{25} nanoclusters. J. Am. Chem. Soc. **136**, 10577 (2014)
56. Yao, Q.F., Yuan, X., Fung, V., Yu, Y., Leong, D.T., Jiang, D.E., Xie, J.P.: Understanding seed-mediated growth of gold nanoclusters at molecular level. Nat. Commun. **8**, 927 (2017)
57. Yao, Q.F., Feng, Y., Fung, V., Yu, Y., Jiang, D.E., Yang, J., Xie, J.P.: Precise control of alloying sites of bimetallic nanoclusters via surface motif exchange reaction. Nat. Commun. **8**, 1555 (2017)
58. Zeng, C., Liu, C., Pei, Y., Jin, R.: Thiol ligand-induced transformation of $Au_{38}(SC_2H_4Ph)_{24}$ to $Au_{36}(SPh\text{-}t\text{-}Bu)_{24}$. ACS Nano. **7**, 6138 (2013)
59. Krishnadas, K.R., Ghosh, A., Baksi, A., Chakraborty, I., Natarajan, G., Pradeep, T.: Intercluster reactions between $Au_{25}(SR)_{18}$ and $Ag_{44}(SR)_{30}$. J. Am. Chem. Soc. **138**, 140 (2016)
60. Krishnadas, K.R., Baksi, A., Ghosh, A., Natarajan, G., Pradeep, T.: Structure-conserving spontaneous transformations between nanoparticles. Nat. Commun. **7**, 13447 (2016)
61. Takano, S., Hirai, H., Muramatsu, S., Tsukuda, T.: Hydride-mediated controlled growth of a bimetallic $(Pd@Au_8)^{2+}$ superatom to a hydride-doped $(HPd@Au_{10})^{3+}$ superatom. J. Am. Chem. Soc. **140**, 12314 (2018)
62. Takano, S., Hirai, H., Muramatsu, S., Tsukuda, T.: Hydrogen-doped gold superatoms $(Au_9H)^{2+}$: synthesis, structure and transformation. J. Am. Chem. Soc. **140**, 8380 (2018)
63. Takano, S., Hasegawa, S., Suyama, M., Tsukuda, T.: Hydride doping to chemically-modified gold-based superatoms. Acc. Chem. Res. **51**, 3074 (2018)
64. Tomihara, R., Hirata, K., Yamamoto, H., Takano, S., Koyasu, K., Tsukuda, T.: Collision-induced dissociation of undecagold clusters protected by mixed ligands $[Au_{11}(PPh_3)_8X_2]^+$ (X = Cl, C ≡ CPh). ACS Omega **3**, 6237 (2018)
65. Angel, L.A., Majors, L.T., Dharmaratne, A.C., Dass, A.: Ion mobility mass spectrometry of $Au_{25}(SCH_2CH_2Ph)_{18}$ nanoclusters. ACS Nano **4**, 4691 (2010)

66. Fields-Zinna, C.A., Sampson, J.S., Crowe, M.C., Tracy, J.B., Parker, J.F., deNey, A.M., Muddiman, D.C., Murray, R.W.: Tandem mass spectrometry of thiolate-protected Au nanoparticles $Na_xAu_{25}(SC_2H_4Ph)_{18-y}(S(C_2H_4O)_5CH_3)_y$. J. Am. Chem. Soc. **131**, 13844 (2009)
67. Yao, Q., Fung, V., Sun, C., Huang, S., Chen, T., Jiang, D., Lee, J.Y., Xie, J.: Revealing isoelectronic size conversion dynamics of metal nanoclusters by a noncrystallization approach. Nat. Commun. **9**, 1979 (2018)
68. Liu, C., Lin, S., Pei, Y., Zeng, X.C.: Semiring chemistry of $Au_{25}(SR)_{18}$: fragmentation pathway and catalytic active site. J. Am. Chem. Soc. **135**, 18067 (2013)
69. Chakraborty, P., Baksi, A., Khatun, E., Nag, A., Ghosh, A., Pradeep, T.: Dissociation of gas phase ions of atomically precise silver clusters reflects their solution phase stability. J. Phys. Chem. C **121**, 10971 (2017)
70. Zhang, H.-F., Stender, M., Zhang, R., Wang, C., Li, J., Wang, L.-S.: Toward the solution synthesis of the tetrahedral Au_{20} cluster. J. Phys. Chem. B **108**, 12259 (2004)
71. Tang, Q., Hu, G., Fung, V., Jiang, D.-E.: Insights into interfaces, stability, electronic properties, and catalytic activities of atomically precise metal nanoclusters from first principles. Acc. Chem. Res. **51**, 2793 (2018)
72. Bertorelle, F., Russier-Antoine, I., Comby-Zerbino, C., Chirot, F., Dugourd, P., Brevet, P.-F., Antione, R.: Isomeric effect of mercaptobenzoic acids on the synthesis, stability, and optical properties of $Au_{25}(MBA)_{18}$ nanoclusters. ACS Omega **3**, 15635 (2018)
73. Bergeron, D.E., Hudgens, J.W.: Ligand dissociation and core fission from diphosphine-protected gold clusters. J. Phys. Chem. C **111**, 8195 (2007)
74. Shvartsburg, A.A., Smith, R.D.: Fundamentals of traveling wave ion mobility spectrometry. Anal. Chem. **80**, 9689 (2008)
75. Daly, S., Choi, C.M., Zavras, A., Krstić, M., Chirot, F., Connell, T.U., Williams, S.J., Donnelly, P.S., Antoine, R., Giuliani, A., Bonačić-Koutecký, V., Dugourd, P., O'Hair, R.A.J.: Gas-phase structural and optical properties of homo- and heterobimetallic rhombic dodecahedral nanoclusters $[Ag_{14-n}Cu_n(C \equiv CtBu)_{12}X]^+$ ($X = Cl$ and Br): ion mobility, VUV and UV spectroscopy, and DFT calculations. J. Phys. Chem. C **121**, 10719 (2017)
76. Ligare, M.R., Baker, E.S., Laskin, J., Johnson, G.E.: Ligand induced structural isomerism in phosphine coordinated gold clusters revealed by ion mobility mass spectrometry. Chem. Commun. **53**, 7389 (2017)
77. Baksi, A., Chakraborty, P., Bhat, S., Natarajan, G., Pradeep, T.: $[Au_{25}(SR)_{18}]_2^{2-}$: a noble metal cluster dimer in the gas phase. Chem. Commun. **52**, 8397 (2016)
78. Chakraborty, P., Baksi, A., Mudedla, S.K., Nag, A., Paramasivam, G., Subramanian, V., Pradeep, T.: Understanding proton capture and cation-induced dimerization of $[Ag_{29}(BDT)_{12}]^{3-}$ clusters by ion mobility mass spectrometry. Phys. Chem. Chem. Phys. **20**, 7593 (2018)
79. Hirata, K., Chakraborty, P., Nag, A., Takano, S., Koyasu, K., Pradeep, T., Tsukuda, T.: Interconversions of structural isomers of $[PdAu_8(PPh_3)_8]^{2+}$ and $[Au_9(PPh_3)_8]^{3+}$ revealed by ion mobility mass spectrometry. J. Phys. Chem. C **122**, 23123 (2018)
80. Shvartsburg, A.A., Jarrold, M.F.: An exact hard-spheres scattering model for the mobilities of polyatomic ions. Chem. Phys. Lett. **261**, 86 (1996)
81. von Helden, G., Hsu, M.-T., Gotts, N., Bowers, M.T.: Carbon cluster cations with up to 84 atoms: structures, formation mechanism, and reactivity. J. Phys. Chem. **97**, 8182 (1993)
82. Larriba, C., Hogan, C.J.: Ion mobilities in diatomic gases: measurement versus prediction with non-specular scattering models. J. Phys. Chem. A **117**, 3887 (2013)
83. Schulz-Dobrick, M., Jansen, M.: Supramolecular intercluster compounds consisting of gold clusters and Keggin anions. Eur. J. Inorg. Chem. **2006**, 4498 (2006)
84. Hirata, K., Yamashita, K., Muramatsu, S., Takano, S., Ohshimo, K., Azuma, T., Nakanishi, R., Nagata, T., Yamazoe, S., Koyasu, K., Tsukuda, T.: Anion photoelectron spectroscopy of free $[Au_{25}(SC_{12}H_{25})_{18}]^-$. Nanoscale **9**, 13409 (2017)
85. Hirata, K., Kim, K., Nakamura, K., Kitazawa, H., Hayashi, S., Koyasu, K., Tsukuda, T.: Photoinduced thermionic emission from $[M_{25}(SR)_{18}]^-$ ($M = Au$, Ag) revealed by anion photoelectron spectroscopy. J. Phys. Chem. C. **123**, 13174 (2019)

86. Tofanelli, M.A., Salorinne, K., Ni, T.W., Malola, S., Newell, B., Phillips, B., Häkkinen, H., Ackerson, C.J.: Jahn-Teller effects in $Au_{25}(SR)_{18}$. Chem. Sci. **7**, 1882 (2016)
87. Akola, J., Walter, M., Whetten, R.L., Häkkinen, H., Grönbeck, H.: On the structure of thiolate-protected Au_{25}. J. Am. Chem. Soc. **130**, 3756 (2008)
88. Kacprzak, K.A., Lehtovaara, L., Akola, J., Lopez-Acevedo, O., Häkkinen, H.: A density functional investigation of thiolate-protected bimetal $PdAu_{24}(SR)^{z}_{18}$ clusters: doping the superatom complex. Phys. Chem. Chem. Phys. **11**, 7123 (2009)
89. Wang, S., Li, Q., Kang, X., Zhu, M.: Customizing the structure, composition, and properties of alloy nanoclusters by metal exchange. Acc. Chem. Res. **51**, 2784 (2018)
90. Hossain, S., Niihori, Y., Nair, L.V., Kumar, B., Kurashige, W., Negishi, Y.: Alloy clusters: precise synthesis and mixing effects. Acc. Chem. Res. **51**, 3114 (2018)
91. Kim, K., Hirata, K., Nakamura, K., Kitazawa, H., Hayashi, S., Koyasu, K., Tsukuda, T.: Elucidating the doping effect on the electronic structure of thiolate-protected silver superatoms by photoelectron spectroscopy. Angew. Chem. Int. Ed. (2019) (in press)
92. Ganteför, G., Eberhardt, W., Weidele, H., Kreisle, D., Recknagel, E.: Energy dissipation in small clusters: direct photoemission, dissociation, and thermionic emission. Phys. Rev. Lett. **77**, 4524 (1996)
93. Schacht, J., Gaston, N.: From the superatom model to a diverse array of super-elements: a systematic study of dopant influence on the electronic structure of thiolate-protected gold clusters. ChemPhysChem **17**, 3237 (2016)
94. Yamazoe, S., Takano, S., Kurashige, W., Yokoyama, T., Nitta, K., Negishi, Y., Tsukuda, T.: Hierarchy of bond stiffnesses within icosahedral-based gold clusters protected by thiolates. Nat. Commun. **7**, 10414 (2016)
95. Hamouda, R., Bellina, B., Bertorelle, F., Compagnon, I., Antoine, R., Broyer, M., Rayane, D., Dugourd, P.: Electron emission of gas-phase $[Au_{25}(SG)_{18}\text{-}6H]^{7-}$ gold cluster and its action spectroscopy. J. Phys. Chem. Lett. **1**, 3189 (2010)
96. Black, D.M., Crittenden, C.M., Brodbelt, J.S., Whetten, R.L.: Ultraviolet photodissociation of selected gold clusters: ultraefficient unstapling and ligand stripping of $Au_{25}(pMBA)_{18}$ and $Au_{36}(pMBA)_{24}$. J. Phys. Chem. Lett. **8**, 1283 (2017)
97. Wu, Z., Gayathri, C., Gil, R.R., Jin, R.: Probing the structure and charge state of glutathione-capped $Au_{25}(SG)_{18}$ clusters by NMR and mass spectrometry. J. Am. Chem. Soc. **131**, 6535 (2009)
98. Beck, R.D., St. John, P., Homer, M.L., Whetten, R.L.: Impact-induced cleaving and melting of alkali-halide nanocrystals. Science **253**, 879 (1991)
99. Johnson, G.E., Laskin, J.: Understanding ligand effects in gold clusters using mass spectrometry. Analyst **141**, 3573 (2016)
100. Baksi, A., Harvey, S.R., Natarajan, G., Wysocki, V.H., Pradeep, T.: Possible isomers in ligand protected Ag_{11} cluster ions identified by ion mobility mass spectrometry and fragmented by surface induced dissociation. Chem. Commun. **52**, 3805 (2016)
101. Yamazoe, S., Tsukuda, T.: X-ray absorption spectroscopy on atomically precise metal clusters. Bull. Chem. Soc. Jpn. **92**, 193 (2019)